Dendritic *atoh1a+* cells serve as transient intermediates during zebrafish Merkel cell development and regeneration

Evan W. Craig[1], Erik C. Black[1,2], Camille E.A. Goo[1], Avery Angell Swearer[1,2], Nathaniel G. Yee[1], Jeffrey P. Rasmussen[1,3,*]

[1] Department of Biology, University of Washington, Seattle, WA, USA
[2] Molecular and Cellular Biology Program, University of Washington, Seattle, WA, USA
[3] Institute for Stem Cell and Regenerative Medicine, University of Washington, Seattle, WA, USA
* Correspondence: rasmuss@uw.edu

Keywords: Ectodysplasin, epidermis, cell motility, somatosensory system, skin organogenesis, piezo2, tp63, microvilli

ABSTRACT

Sensory cells often adopt specific morphologies that aid in the detection of external stimuli. Merkel cells encode gentle touch stimuli in vertebrate skin and adopt a reproducible shape characterized by spiky, actin-rich microvilli that emanate from the cell surface. The mechanism by which Merkel cells acquire this stereotyped morphology from basal keratinocyte progenitors is unknown. Here, we establish that dendritic Merkel cells (dMCs) express *atonal homolog 1a (atoh1a)*, extend dynamic filopodial processes, and arise in transient waves during zebrafish skin development and regeneration. We find that dMCs share molecular similarities with both basal keratinocytes and Merkel cells, yet display mesenchymal-like behaviors, including local cell motility and proliferation within the epidermis. Furthermore, dMCs can directly adopt the mature, microvilliated Merkel cell morphology through substantial remodeling of the actin cytoskeleton. Loss of Ectodysplasin A signaling alters the morphology of dMCs and Merkel cells within specific skin regions. Our results show that dMCs represent an intermediate state in the Merkel cell maturation program and identify Ectodysplasin A signaling as a key regulator of Merkel cell morphology.

INTRODUCTION

Organ development and function require that constituent cells adopt precise shapes. For example, epithelial cells often develop elaborate actin-based membrane protrusions integral to organ function, such as the brush border of intestinal enterocytes or the stereocilia of inner ear hair cells (reviewed by Sharkova et al., 2023). Defects in the morphogenesis of actin-based protrusions are linked to a variety of diseases, including colorectal cancer and deafness. Thus, elucidating the mechanisms of how epithelial cells adopt specific shapes is relevant to understanding both the basis for organ function and the etiology of human pathologies.

Merkel cells (MCs) are mechanosensory epidermal cells that interact with somatosensory neurites to form the MC-neurite complex, which mediates detection of gentle touch stimuli (reviewed by Woo et al., 2015). MCs populate diverse vertebrate skin compartments, including human plantar and palmar skin, mouse hairy and glabrous skin, and teleost facial and trunk skin (reviewed by Hartschuh et al., 1986; Whitear, 1989). MCs have a remarkably consistent morphology across these diverse vertebrate skin types. The core morphological features of MCs include a small and spherical cell body, a high nuclear-to-cytoplasmic ratio, and the presence of neurosecretory granules (Hartschuh et al., 1986; Whitear, 1989). But perhaps the most striking morphological feature of MCs are the numerous actin-rich microvilli that emanate off the cell surface, giving MCs a “mace-like” morphology (Hartschuh et al., 1986; Lane and Whitear, 1977; Sekerková et al., 2004; Takahashi-Iwanaga, 2003; Takahashi-Iwanaga and Abe, 2001; Toyoshima et al., 1998; Whitear and Lane, 1981).

The precise and reproducible cell shape of MCs has been proposed to impact their sensory function (Garant et al., 1980; Takahashi-Iwanaga, 2003; Takahashi-Iwanaga and Abe, 2001; Toyoshima et al., 1998; Yamashita et al., 1993); however, it is unknown how MCs acquire this stereotyped morphology. Cre-based lineage tracing experiments indicate that MCs derive from basal keratinocyte precursors in both mammalian and zebrafish skin (Brown et al., 2023; Morrison et al., 2009; Van Keymeulen et al., 2009). While these experiments begin to address MC progenitor identity, they fail to shed light on how cells within this lineage lose basal keratinocyte characteristics and adopt the hallmark MC morphology. A deeper understanding of the MC lineage may shed light on the origins of Merkel cell carcinoma, an aggressive skin cancer of unclear cellular origin (reviewed by Becker et al., 2017; Harms et al., 2018).

Interestingly, several histological observations support the presence of cellular intermediates in the MC lineage. First, ultrastructural studies identified “transitional cells” that exhibit characteristics of both keratinocytes and MCs, including fine cytoplasmic filaments and dense-core granules, respectively (English, 1974; English, 1977; Garant et al., 1980; Tachibana and Ishizeki, 1981; Tachibana and Nawa, 1980). Second, immunostaining for two MC markers—cytokeratins 18 and 20—revealed cells with oblong or dendritic morphologies in developing human plantar skin, human and rodent oral mucosa, and murine touch domes (Kim and Holbrook, 1995; Moll et al., 1984; Nakafusa et al., 2006; Tachibana et al., 1997; Tachibana et al., 1998). Although these heterogeneously shaped cells have been referred to as dendritic MCs (dMCs), it is unknown whether dMCs represent a developmentally immature MC state or a

75 functionally distinct subpopulation of neuroendocrine cells (reviewed by Xiao et al., 2014). Live-
76 cell imaging of MC development would be the most direct way to distinguish these possibilities.
77 However, to date, technical limitations of mammalian systems have precluded visualization of
78 dMC or MC dynamics in living animals.
79
80 We recently established zebrafish as an *in vivo* model for MC studies (Brown et al., 2023). Here,
81 we leverage the optical accessibility of zebrafish skin to directly visualize individual cell
82 behaviors during the MC maturation process. By visualizing key stages of skin organogenesis
83 and regeneration using an F-actin reporter expressed in MCs, we describe a morphologically
84 distinct population of epidermal cells that shares characteristics with transitional cells and dMCs
85 observed in other types of vertebrate skin. Importantly, we document the direct maturation of
86 dMCs into MCs through cytoskeletal rearrangements. Furthermore, we show that Ectodysplasin
87 A (Eda) signaling is required for MCs to develop microvilli within trunk skin. Together, our results
88 provide the first *in vivo* characterizations of MC precursor states and identify Eda signaling as a
89 key regulator of zebrafish MC morphogenesis.
90
91 **RESULTS**
92
93 ***A transient, morphologically distinct population of keratinocyte-derived* atoh1a+ *cells***
94 ***emerges during skin development***
95
96 Staging of zebrafish post-embryonic development relies on standard length (SL) in millimeters,
97 with sexual maturity attained ~18 mm SL (Parichy et al., 2009). Cells with the prototypical MC
98 morphology—spherical with actin-rich, microvillar protrusions of ~1-2 microns in length—
99 populate several adult zebrafish skin compartments, including trunk skin (**Figure 1A,B**; (Brown
100 et al., 2023)). *Atonal homolog 1* (*Atoh1*) encodes a transcription factor necessary and sufficient
101 for murine MC development (Morrison et al., 2009; Ostrowski et al., 2015; Van Keymeulen et
102 al., 2009). Zebrafish *atoh1a* is an ortholog of murine *Atoh1*, and zebrafish MCs express
103 reporters inserted into the upstream region of the *atoh1a* locus (Brown et al., 2023). Using a
104 nuclear localized *atoh1a* reporter to label MCs, we previously found that trunk MCs begin to
105 appear during the onset of squamation (scale formation) at approximately 9 mm SL and rapidly
106 increase in density from 10-15 mm SL (Brown et al., 2023). As this nuclear reporter did not
107 allow for visualization of cell shapes, it is unclear whether morphological heterogeneity exists
108 within developing zebrafish MCs, including the possible presence of dMCs.
109
110 To assess MC morphology during squamation, we conducted a similar developmental staging
111 time course using *Tg(atoh1a:lifeact-egfp)*, which expresses a filamentous actin (F-actin) reporter
112 in MCs, allowing detailed visualization of the MC actin cytoskeleton *in vivo* (**Figure 1C**; (Brown
113 et al., 2023)). To simultaneously visualize scales, we stained animals with Alizarin Red S, which
114 labels the calcified scale matrix. Like our previous observations in adults, we identified cells with
115 the prototypical MC morphology at late juvenile and adult stages (**Figure 1F-H,** arrowheads).
116 Interestingly, we also observed a second population of *atoh1a*+ cells with weaker transgene
117 signal and highly variable morphologies, characterized by ovoid cell bodies and long, filopodial-
118 like actin-rich protrusions (**Figure 1D-G,** arrows). For consistency with the literature (Boot et al.,

1992; Kim and Holbrook, 1995; Moll et al., 1984; Nakafusa et al., 2006; Tachibana et al., 1997; Tachibana et al., 1998), we hereafter refer to these cells as dMCs, although we note that whether dMCs are related to MCs or represent an alternative fate has not been established. Manual cell counting from our imaging dataset revealed dMCs appeared in highest frequency and density at 10-15 mm SL, when scales expand and total MC density rapidly increases (**Figure 1I-K**). Next, we quantified *atoh1a* cell shapes at two different developmental stages by assigning circularity and roundness values to thresholded images from our dataset. We defined "circular" cells as those having circularity and roundness values >0.7. We found that 95.3% of *atoh1a+* cells in adult skin fell into the circular category, likely representing the mature, microvilliated MC type (**Figure 1M,N**). By contrast, only 71.1% of *atoh1a+* cells in juvenile skin fell into the circular category, with numerous *atoh1a+* cells adopting more oblong and less round shapes. (**Figure 1L,N**). Thus, our results indicate that a morphologically distinct population of *atoh1a+* cells transiently populates the trunk skin during squamation.

Using a tamoxifen-inducible Cre driver expressed in basal keratinocytes [*TgBAC(ΔNp63:Cre-ERT2)*; (Brown et al., 2023)] and a quasi-ubiquituous Cre reporter transgene [*Tg(actb2:LOXP-BFP-LOXP-DsRed)*; (Kobayashi et al., 2014)], we previously found that zebrafish MCs derive from *ΔNp63*-expressing basal keratinocytes (Brown et al., 2023). To determine if basal keratinocytes also give rise to dMCs, we treated *TgBAC(ΔNp63:Cre-ERT2); Tg(actb2:LOXP-BFP-LOXP-DsRed); Tg(atoh1a:lifeact-egfp)* embryos with 4-OHT to induce Cre-ERT2 activity at 1 day post-fertilization (dpf). This resulted in permanent DsRed expression in basal keratinocytes and their cellular derivatives. We then raised animals to squamation stages. Due to transgene mosaicism and/or incomplete Cre-ERT2 activation, not all basal keratinocytes expressed DsRed (**Figure 1O**). Along with DsRed+ MCs (**Figure 1O'''**), we observed that a subset of dMCs in juvenile skin were DsRed+ (**Figure 1O'-O''**). Interestingly, we often identified DsRed+ dMCs at a distance from the nearest DsRed+ basal keratinocyte (**Figure 1O**). These findings demonstrate a basal keratinocyte origin for dMCs and suggest they may be motile.

dMCs are the primary* atoh1a+ *cell type during early stages of skin regeneration

Our identification of dMCs during squamation prompted us to hypothesize that dMCs may also appear during specific stages of scale regeneration. To induce scale regeneration, we performed scale "plucking" with fine forceps to remove both the bony scale and overlying epidermis containing MCs (**Figure 2A**). Scale removal triggers a wound healing response from neighboring keratinocytes, which migrate from surrounding, non-injured scales to cover the denuded area within hours (Richardson et al., 2016). Over the course of several days, keratinocytes then proliferate and reestablish a stratified epidermis (Richardson et al., 2016), while dermal osteoblasts proliferate and undergo hypertrophy to regenerate the bony scale (Aman et al., 2018; Cox et al., 2018; De Simone et al., 2021; Iwasaki et al., 2018; Sire et al., 1997).

To determine whether MCs populated the regenerating scale epidermis, we plucked scales from animals expressing *Tg(atoh1a:Lifeact-egfp)* and *Tg(sp7:mCherry)* (Singh et al., 2012), a reporter for scale-forming osteoblasts (**Figure 2A,B**). As expected, scales underwent

163 substantial regeneration within the first 7 days post-pluck (dpp) (**Figure 2B-E**). *atoh1a*+ cells
164 appeared above regenerating scales beginning at 2 dpp and rapidly increased in density until 7
165 dpp, after which the density plateaued (**Figure 2F-J**). Strikingly, dMCs comprised ~95% of the
166 *atoh1a*+ cells present at 2 dpp (**Figure 2G,G',K**) and ~45% of the *atoh1a*+ cells at 3 dpp
167 (**Figure 2H,K**). After 3 dpp, the proportion of dMCs gradually decreased, with MCs becoming
168 the predominant *atoh1a*+ cell type at later stages of regeneration (**Figure 2I,K**)
169
170 dMCs and MCs on regenerating scales could arise from either *de novo* production or movement
171 of pre-existing *atoh1a*+ cells from surrounding, uninjured regions of epidermis. To distinguish
172 between these possibilities, we irreversibly photoconverted *atoh1a*+ cells expressing a nuclear
173 localized version of the photoconvertible protein Eos [*Tg(atoh1a:nls-Eos);* (Pickett et al., 2018)]
174 and then plucked scales (**Figure 2L,M**). In this experimental paradigm, pre-existing *atoh1a*+
175 cells contain both photoconverted and non-photoconverted nls-Eos, whereas newly
176 differentiating *atoh1a*+ cells contain only non-photoconverted nls-Eos. Notably, at 2 and 3 dpp
177 the epidermis contained many newly differentiated cells with oval nuclear morphologies that
178 likely represented dMCs **(Figure 2N,O,Q)**. By 7 dpp, nearly all *atoh1a*+ cells were newly derived
179 (**Figure 2P,Q)**. Based on these results, we concluded that skin injury triggers *de novo*
180 production of dMCs and MCs within the trunk epidermis and that early stages of epidermal
181 regeneration are associated with a high proportion of dMCs. Thus, dMCs are a transient
182 *atoh1a*+ cell type during both skin development and regeneration.
183
184 ***dMCs exhibit molecular features of both basal keratinocytes and MCs***
185
186 To characterize the molecular and cellular properties of regenerating dMCs, we focused on 5
187 dpp, a timepoint that contains a mix of dMCs and MCs (**Figure 2K**). We first assayed
188 expression of Tp63, a transcription factor critical in epidermal development and highly
189 expressed in basal keratinocytes (Bakkers et al., 2002; Guzman et al., 2013; Lee and
190 Kimelman, 2002; Rangel-Huerta et al., 2021) (**Figure 3B, asterisks**). Immunostaining revealed
191 that MCs did not express detectable levels of Tp63 (**Figure 3A-A'**). By contrast, dMCs exhibited
192 significantly higher levels of Tp63 staining than MCs, albeit at lower levels than basal
193 keratinocytes, with ~75% of dMCs staining positive for Tp63 (**Figure 3B-C**). Thus, dMCs
194 express Tp63 at intermediate levels relative to basal keratinocytes and MCs.
195
196 Given our finding that dMCs expressed *atoh1a*, we postulated that dMCs might share additional
197 molecular properties with MCs. MCs express markers of neuroendocrine and mechanosensory
198 function, such as synaptic vesicle glycoprotein 2 (SV2) and the mechanosensitive cation
199 channel Piezo2, respectively. Consistent with previous observations during ontogeny (Brown et
200 al., 2023), we found that regenerated MCs expressed SV2 (**Figure 3D-D'**). SV2 staining of
201 dMCs in regenerating skin revealed a mix of SV2+ and SV2– dMCs (**Figure 3E-E'**). We
202 quantified the SV2 fluorescence intensity from dMCs with detectable signal and found dMCs
203 displayed lower SV2 levels than MCs (**Figure 3F**). Hybridization chain reaction (HCR) staining
204 for *piezo2* labeled both MCs (**Figure 3G-G', arrowhead**) and dMCs (**Figure 3G-G', arrow**) in
205 regenerating skin. Analysis of the *piezo2* signal revealed slightly lower levels in dMCs compared
206 to MCs (**Figure 3H**). In summary, regenerating dMCs display molecular properties that overlap

with both basal keratinocytes and MCs, suggesting they may represent a transitional or immature MC.

MC and dMC protrusions are dynamic and differentially polarized

Apart from previous reports that tracked MC turnover over the course of days or weeks by imaging cytoplasmic or nuclear reporters (Brown et al., 2023; Wright et al., 2017), little is known about the *in vivo* dynamics of MCs. Given the differences in cell shapes between dMCs and MCs during development and regeneration, we sought to compare the dynamics and polarities of the actin cytoskeleton in these two populations. To this end, we mounted and intubated *Tg(atoh1a:lifeact-egfp)* animals and performed live-cell confocal microscopy of fully intact skin over several hours. Imaging of MCs in adult zebrafish revealed strong Lifeact-EGFP signal in microvilli as expected (**Figure 4A, arrowhead**). We captured numerous microvillar reorientation, retraction, and extension events occurring in all MCs (**Figure 4A-A''''; Movie 1**), suggesting previously unappreciated MC microvillar dynamics. MC microvilli rarely extended >3 microns from the membrane and often appeared to coalesce or merge together, although we lacked the resolution to reliably characterize these merging events. Despite these microvillar dynamics, the MC cortex remained spherical during imaging (**Figure 4A-A''''**). By analyzing reconstructed cross-sections of MC microvilli in animals also expressing a Cdh1 (E-cadherin) knock-in reporter to label keratinocyte membranes [Cdh1-tdTomato; (Cronan et al., 2018)] (**Figure 4C**), we found the majority of MC microvilli extended in basal keratinocyte-facing or lateral directions, whereas periderm-facing processes were less common (**Figure 4D,D',F,G**).

In contrast to MC microvilli, imaging of dMCs in juveniles revealed long, thin Lifeact-EGFP+ protrusions that routinely exceeded 10 microns in length and in extreme cases exceeded 25 microns (**Figure 4B-B'''', arrowheads**). dMCs dynamically rearranged both their protrusions and cell cortex (**Figure 4B-B''''; Movie 2**). dMC protrusions tended to coalesce and extend from one end of the cell, with the opposite side of the dMC having few or no protrusions (**Figure 4B''**). The majority of dMC protrusions extended in lateral or periderm-facing directions, whereas basal keratinocyte-facing processes were less common (**Figure 4E,E',F,G).** Reconstructed cross-sections also revealed that MCs tended to reside just below the periderm, whereas dMCs were commonly in lower strata (**Figure 4D',E',H**). Thus, our observations indicate MCs and dMCs occupy different strata of the epidermis and utilize dynamic actin-based protrusions that are of distinct sizes and polarities.

dMCs are mesenchymal-like cells that directly mature into MCs

We wondered how MCs and dMCs behaved during periods of development when MC density greatly increases in the trunk skin (10-15 mm SL, **Figure 1J,K**). Based on their association with somatosensory neurites and desmosome-like contacts with keratinocytes, we hypothesized that MCs would be relatively immotile. By contrast, our Cre lineage tracing data (**Figure 1O**) and observations of dMC protrusion dynamics and polarity (**Figure 4**), led us to hypothesize that dMCs may migrate within the epidermis.

To characterize MC and dMC motility, we intubated *Tg(atoh1a:lifeact-egfp)* juveniles and imaged fields of view containing MCs and dMCs over 6 h (**Figure 5A, Movie 3**). Consistent with our hypotheses, cell tracking revealed that MCs were largely immotile, whereas dMCs migrated laterally within the epidermis (**Figure 5A, insets)**. dMC motility was highly variable: On average, dMCs migrated 2.4 µm/hr during imaging, but some moved upwards of 8 µm/hr, while others remained stationary (**Figure 5B**). By contrast, MCs were immotile, with an average displacement of 0.8 µm/hr, which likely reflects imaging drift (**Figure 5B**). dMCs were most motile when adopting elongated, ovoid cell bodies with long, unipolar protrusions at one end of the cell (**Figure 5E, pink arrowheads**). By contrast, dMCs with multipolar protrusions were largely immotile (**Figure 5E, orange arrowheads**). Although the majority of dMCs traveled in a persistent or linear manner (**Figure 5C**), dMCs had a significantly reduced track displacement compared to total distance traveled (**Figure 5D**), suggesting that dMCs migrate directionally but often switch directions. Consistent with this notion, dMC-dMC or dMC-MC contacts resulted in lateral dMC movement away from the contact (**Movie 4**). Together these observations suggest that MCs are immotile, epithelial-like cells, whereas dMCs are motile, mesenchymal-like cells that undergo contact inhibition upon encountering another *atoh1a*+ cell.

MCs are generally considered post-mitotic (Merot and Saurat, 1988; Moll et al., 1996; Vaigot et al., 1987; Weber et al., 2023; Wright et al., 2017). Indeed, we did not observe instances of MC cell division in our live-imaging of either homeostatic juvenile or regenerating adult skin. By contrast, dMCs divided in both contexts (**Figure S1A-C**). During cell division, dMCs resorbed their protrusions, developed a smooth actin-rich membrane, and underwent cytokinesis to generate two daughter dMCs, which established protrusions orthogonal to the division plane and migrated away from each other (**Figure S1A-C; Movie 5)**. Due to its experimental tractability, we quantified dMC and MC cell division frequency during skin regeneration. To this end, we injected 5-ethynyl-2´-deoxyuridine (EdU), a thymidine analog incorporated into DNA during active DNA synthesis, at 4 dpp and fixed and stained scales at 5 dpp (**Figure S1D**). In this experimental paradigm, no MCs stained positive for EdU, whereas 65% of dMCs stained positive for EdU (**Figure S1E,F**). Thus, in addition to exhibiting differences in motility, dMCs and MCs show contrasting cell cycle states.

Our findings that dMCs exhibited characteristics of both basal keratinocytes and MCs (**Figure 3**) suggested they may represent an intermediate cellular state between these two cell types. Indeed, during our live-imaging of juvenile and regenerating adult skin, we observed a small subset of dMCs (n>10) withdraw their long protrusions, round up their cell body, and rapidly extend microvilli reminiscent of the mature “mace-like” MC morphology (**Figure 5F; Movies 6,7**). These observations are consistent with the direct maturation of a dMC into a MC. In rare instances (n=2), we observed the reciprocal process, i.e., the reversion of a MC into a dMC-like morphology (**Figure 5G; Movie 8**), suggesting that some MCs can switch between cell states. Thus, based on these observations, we conclude that dMCs are capable of cell migration, cell division, and direct maturation into MCs (**Figure 5H**).

Genetic loss of Eda results in altered dMC and MC morphologies in trunk skin

294 Eda signaling promotes the development of diverse vertebrate skin appendages (reviewed by
295 Sadier et al., 2014), including zebrafish scales (Harris et al., 2008). We previously reported that
296 zebrafish homozygous for a presumptive null *eda* allele (*eda*$^{dt1261/dt1261}$, hereafter *eda*$^{-/-}$)
297 displayed reduced MC density within the trunk, but not facial, epidermis (Brown et al., 2023).
298 We postulated that Eda signaling may also promote the morphological maturation of MCs. To
299 address this hypothesis, we incrossed *eda*$^{+/-}$ adults and used *Tg(atoh1a:lifeact-egfp)* localization
300 to compare MC morphology between homozygous mutants and sibling controls. As expected,
301 control trunk MCs developed a typical "mace-like" morphology decorated by microvilli (**Figure**
302 **6A-A''',G**). By contrast, we observed a striking and highly penetrant loss of MC microvillar
303 structures along the trunk of *eda*$^{-/-}$ mutants (**Figure 6B-B''',G**). In *eda*$^{-/-}$ trunk MCs, Lifeact-
304 EGFP signal accumulated near the membrane in a ring-like fashion (**Figure 6B', arrowhead**),
305 reminiscent of the morphology of dMCs during cell division (**Figure S1A-C**). The few MC
306 microvilli that formed in *eda*$^{-/-}$ trunk MCs were short and thin, making them difficult to resolve
307 with confocal microscopy. To determine whether Eda globally regulated MC morphology
308 throughout the skin, we imaged MCs in the corneal epidermis, which is not squamated. This
309 analysis revealed corneal MCs with similar microvilli-rich morphologies in *eda*$^{-/-}$ mutants and
310 siblings (**Figure 6C-D,G**). Finally, to determine whether loss of Eda signaling also impacted
311 dMC morphology, we compared the maximum protrusion length of dMCs in *eda*$^{-/-}$ mutants and
312 controls and found that mutant dMCs had significantly longer protrusions (**Figure 6E,F,H;** *eda*$^{-/-}$
313 dMC mean lengths = 16.3 μm, siblings = 8.7 μm). In extreme cases, dMC protrusions reached
314 almost 40 microns in length in *eda*$^{-/-}$ trunk epidermis (**Figure 6F**). Together, these results
315 indicate that Eda is necessary for the normal morphologies of dMCs and MCs specifically within
316 the trunk skin compartment.
317
318
319 **DISCUSSION**

320 The defining morphological features of MCs allows for their identification across diverse types of
321 vertebrate skin (Hartschuh et al., 1986; Whitear, 1989). How MCs acquire this precise
322 morphology during skin development or regeneration is unknown. While basal keratinocytes
323 have been identified as MC progenitors in mammalian and zebrafish skin, intermediate steps in
324 the MC lineage progression remain poorly understood. Previous histology-based experiments
325 noted transitional cells that could serve as cellular intermediates during MC maturation (English,
326 1974; English, 1977; Garant et al., 1980; Tachibana and Ishizeki, 1981; Tachibana and Nawa,
327 1980). However, these studies lacked the temporal resolution to rigorously establish a
328 relationship between transitional cells and MCs. Here, we directly address this knowledge gap
329 by using the optical accessibility of zebrafish skin to track the emergence of MCs during
330 development and regeneration. Our results support a model in which dMCs emerge in lower
331 epidermal strata and migrate locally within the epidermis. Their migration occurs both laterally,
332 presumably due to their lateral-facing actin-rich membrane protrusions, and vertically within the
333 epidermis. As they mature in superficial strata, dMCs reorganize their actin cytoskeleton to
334 elaborate polarized microvilli, thereby adopting the terminal mace-like morphology characteristic
335 of MCs (**Figure 5H**).

336 ***A transient cell state during development and regeneration***

337 We observed that dMCs appeared transiently during a period of skin organogenesis associated
338 with dermal appendage growth along the trunk. dMC frequency peaked during a time of rapid
339 increase in MC density. These findings closely mirror previous studies in other vertebrates. For
340 instance, the “dendritic:globular” MC ratio sharply decreased in embryonic and human fetal
341 palmar skin prior to the peak of MC density (Kim and Holbrook, 1995). Furthermore, our lineage
342 tracing identified basal keratinocytes as dMC precursors, supporting previous ultrastructural
343 findings that suggested basal keratinocytes give rise to transitional cells (English, 1974; English,
344 1977; Garant et al., 1980; Tachibana and Ishizeki, 1981; Tachibana and Nawa, 1980). However,
345 since those TEM studies did not reconstruct transitional cell morphology, any relationship
346 between transitional cells and dMCs has remained unclear. Based on our lineage tracing and
347 morphological data, we propose that dMCs and transitional cells likely represent similar cellular
348 intermediates. However, dMCs may represent just one of several intermediate states between
349 basal keratinocytes and MCs, each with their own characteristics as previously suggested
350 (Tachibana and Ishizeki, 1981).

351 Severe skin wounds, such as burns, can alter sensory perception, thereby degrading patient
352 quality of life (reviewed by Girard et al., 2017). Human MC regeneration after injury appears
353 poor (Stella et al., 1994), although engineered skin grafts present a promising avenue (Hahn et
354 al., 2019). Studies of the mechanisms of MC regeneration in model organisms may inform
355 improved wound healing treatments. Previous work in mammalian models found that MCs
356 regenerate after peripheral nerve crush (Burgess et al., 1974; Nurse et al., 1984), cauterization
357 of touch domes (Horch, 1982), full thickness wounds (Tachibana and Ishizeki, 1981), or
358 repeated skin shaving (Weber et al., 2023; Wright et al., 2017). We found that scale plucking
359 induced a high proportion of dMCs during the early phase of scale regeneration and that MC
360 density ultimately recovered to pre-injury levels. Using a photoconvertible reporter, we
361 established that MCs in regenerated epidermis form predominantly due to *de novo* regeneration
362 rather than migration from surrounding epidermal reservoirs. Due to the rapid kinetics, scale
363 pluck presents a tractable model for reliably triggering dMC/MC production after cutaneous
364 injury.

365 We used scale pluck as an approach to reliably induce dMCs and quantitatively characterize
366 their molecular properties during regeneration. We found that dMCs expressed the basal
367 keratinocyte marker Tp63 at intermediate levels relative to MCs (low) and basal cells (high). We
368 found that dMCs frequently expressed the MC markers *piezo2* and SV2, albeit at levels lower
369 than MCs. Together these data lend further support to the notion that transitional cells and
370 dMCs are one and the same, and suggest that dMCs may represent MC precursors.
371 Additionally, *piezo2* expression in dMCs suggests they may have the capacity for
372 mechanosensory function. Examining whether mechanosensation impacts any of the dMC
373 behaviors described here is an exciting area for future study.

374 ***Dynamic cellular behaviors of dMCs and MCs***

375 The microvilli of several cell types, including cultured renal and immune cells, exhibit dynamic
376 motility (Cai et al., 2017; Meenderink et al., 2019). However, to our knowledge, no live-cell
377 imaging of MC microvilli has been reported. Our *in vivo* imaging revealed that MC microvilli were

dynamic and frequently extended, rearranged, or retracted. Our observations are consistent with the lack of desmosomes along MC microvilli, a feature noted in a wide range of vertebrates and skin compartments (Düring and Andres, 1976; Garant et al., 1980; Halata, 1975; Hashimoto, 1972; Iggo and Muir, 1969; Landmann and Halata, 1980; Takahashi-Iwanaga and Abe, 2001). We further found that MC microvilli were polarized in lateral- or basal keratinocyte-facing orientations. Intriguingly, lamprey microvilli face both superficial and basal strata (Daghfous et al., 2020; Takahashi-Iwanaga and Abe, 2001), whereas MC microvilli within cat touch domes face superficial strata (Iggo and Muir, 1969). These observations suggest malleability of MC microvilli polarity across vertebrates. If microvilli are involved in MC function as previously proposed (Garant et al., 1980; Takahashi-Iwanaga, 2003; Takahashi-Iwanaga and Abe, 2001; Toyoshima et al., 1998; Yamashita et al., 1993), reconciling microvillar dynamics and polarity with MC function will be an interesting area for future exploration.

Our live imaging further revealed a number of previously unrecognized behaviors of dMCs, many of which are properties of mesenchymal cells. First, we found that dMCs elaborate long, thin actin-rich protrusions, reminiscent of protrusions previously observed with cytokeratin 20 staining in gerbil palate (Tachibana et al., 1997). These protrusions extended from lateral-facing membranes and interdigitated between basal and suprabasal keratinocytes. Second, in contrast to the immotile MCs, we observed that dMCs migrated laterally within the epidermis. dMC migration correlated with the presence of unipolar protrusions, whereas dMCs with multipolar protrusions were largely stationary. Intriguingly, dMCs with similar shapes (termed unipolar and globular) were previously noted in adult human oral mucosa (Tachibana et al., 1998). Future work is needed to dissect the molecular composition of dMC protrusions to determine whether they are similar to filopodial/filopodial-like protrusions observed in other contexts. Third, we observed that dMC-dMC or dMC-MC contacts resulted in repulsive behaviors, akin to contact inhibition. As zebrafish MCs are exclusively solitary cells, we speculate that this behavior may promote cell dispersion. Fourth, we observed that dMCs could divide, generating two daughter cells with similar morphologies and behaviors. This suggests that at least a subset of dMCs may be transient amplifying cells. Finally, and perhaps most significantly, we observed in rare instances dMCs could mature into MCs by retracting their protrusions, adopting a spherical cell body, and elaborating microvilli. This provides the first direct evidence that dMCs can serve as MC precursors. Although we do not know yet what cues this maturation, it appears to involve a transition from a mesenchymal-like to an epithelial-like state.

Ectodysplasin and MC maturation

In contrast to the well-studied stereocilia of hair cells (reviewed by Barr-Gillespie, 2015), virtually nothing is known about molecular control of MC microvilli assembly. Nevertheless, both hair cell stereocilia and MC microvilli contain a core of parallel actin bundles and share expression of at least one actin bundling protein (Sekerková et al., 2004; Sekerková et al., 2006). We previously found that Eda signaling was partially necessary for MC development along the trunk skin and that *eda* mutants had a reduced rate of MC production (Brown et al., 2023). Here, we extended these studies by examining the morphology of dMCs and MCs in *eda* loss of function mutants. Surprisingly, we found that most MCs completely lacked microvilli in *eda* mutants, a novel MC phenotype to our knowledge. This observation indicates Eda functions upstream of a MC

microvillar program; dissecting the connections between Eda signaling, MC microvilli, and MC function represent important areas for further study, and *eda* mutants offer a promising system to test MC sensory ability in the absence of microvilli. Furthermore, we found that dMCs developed hyperextended protrusions in *eda* mutants. One interpretation of these data is that dMC protrusion depends on local dMC and/or MC density. Addressing this possibility will require rigorous spatial analysis and experimental manipulation independent of Eda signaling.

In summary, we use the live imaging advantages of zebrafish to describe the dynamic cell behaviors of dMCs and MCs during development and regeneration. We establish that dMCs represent an intermediate cell state between basal keratinocytes and MCs. We further identify Eda signaling as essential for the regional morphogenesis of MCs. Finally, we speculate that the mesenchymal-like behaviors of dMCs may have relevance for understanding the genesis of Merkel cell carcinoma.

MATERIALS AND METHODS

Animals

Zebrafish and developmental staging

Zebrafish were housed at 26-27℃ on a 14/10 h light cycle. Zebrafish of either sex were used. Strains used: AB (Wild-Type), *(cdh1-tdTomato)*^{xt18} (Cronan et al., 2018), *Tg(atoh1a:nls-Eos)*^{w214Tg} (Pickett et al., 2018), *Tg(atoh1a:lifeact-EGFP)*^{w259Tg}, *TgBAC(ΔNp63:Cre-ERT2)*^{w267Tg} (Brown et al., 2023), *Tg(actb2:LOXP-BFP-LOXP-DsRed)*^{sd27Tg} (Kobayashi et al., 2014), *Tg(Ola.Sp7:mCherry-Eco.NfsB)*^{pd46Tg} [referred to as *Tg(sp7:mCherry)*] (Singh et al., 2012), and *eda*^{dt1261} (Harris et al., 2008). All zebrafish experiments were approved by the Institutional Animal Care and Use Committee at the University of Washington (protocol #4439-01).

To control for differences in growth rates, zebrafish post-embryonic development was staged based on standard length (SL) (Parichy et al., 2009). SL of fish was measured using the IC Measure software (The Imaging Source) on images captured on a Stemi 508 stereoscope (Zeiss) equipped with a DFK 33UX264 camera (The Imaging Source). *eda* mutants and siblings were sorted by visible phenotype starting at 7 mm SL. Mutants were grown separately from siblings.

Induction of TgBAC(ΔNp63:Cre-ERT2) with 4-OHT

To activate recombination with Cre-ERT2, 1 dpf *TgBAC(ΔNp63:Cre-ERT2)*; *Tg(actb2:LOXP-BFP-LOXP-DsRed); Tg(atoh1a:lifeact-EGFP)* embryos were treated with 10 μM 4-OHT for 24 hr and screened for successful recombination at 3-5 dpf as evidenced by DsRed+ epidermal cells. 4-OHT was prepared as described (Felker et al., 2016).

Scale pluck

A scale pluck protocol was used either to collect scales for immunofluorescence or to induce scale regeneration. To prepare fish for scale pluck, fish were anesthetized in 0.006-0.012% buffered MS-222 (MilliporeSigma, Cat #: E10521) diluted in system water until a surgical plane of anesthesia was reached. Anesthetized fish were moved under a dissecting microscope and placed on the lid of a petri dish. Dumont #5 forceps were used to pluck scales from the trunk in a posterior to anterior procession. Fish were then returned to system water and monitored for full recovery.

Imaging

Scale regeneration time course

Scales were plucked from adult *Tg(atoh1a:lifeact-egfp);Tg(sp7:mcherry)* zebrafish as described above. To facilitate subsequent imaging, the two rows along the midline were plucked. Plucked fish were returned to the recirculating system and imaged using confocal microscopy at the indicated dpp. 1.5x and 8x images were collected for quantification and downstream analyses.

Whole animal photoconversion

Prior to scale removal, *Tg(atoh1a:nls-Eos)* zebrafish were exposed to light from a UV LED flashlight (McDoer) for 15 min in a reflective chamber constructed from a styrofoam box lined with aluminum foil. A similar lateral region of the trunk was imaged over subsequent days identified by approximate body position below the dorsal fin and relative to underlying pigment stripes.

Confocal imaging

Short-term live imaging of juvenile and adult zebrafish was achieved by anesthetizing fish in 0.006-0.012% MS-222 diluted in system water for ~5 min. Once the fish was immobilized, it was mounted in a custom imaging chamber and the fish body was secured by carefully adding molten 1% agarose in system water. Agarose was not applied to the trunk region where imaging occurred or near the gills and mouth of the fish to ensure survival. Agarose embedded fish were then covered with MS-222 solution and placed under an A1R MP+ scanhead mounted on a Ni-E upright microscope (Nikon). Except where noted otherwise, a 16x water dipping objective (N.A. 0.8) was used for z-stack acquisition and images were post-processed using the Denoise.ai function in NIS-Elements (Nikon). For short-term imaging, fish were taken off the microscope after a maximum 25 min of image collection and returned to system water for recovery.

Long-term live imaging of juvenile zebrafish was achieved through an intubation-based protocol that delivered tricaine-water to immobilized zebrafish using a peristaltic-pump, similar to Xu et al. (2015). In brief, fish were anesthetized in MS-222 for 8-10 min until gill movement became very slow. Fish were transferred to a custom imaging chamber and embedded with 1% agarose as described above. Continuous delivery of MS-222 was achieved by using forceps to gently insert polyethylene tubing (Becton Dickinson #427421 or #427400) into the fish's mouth. This delivery line was held in place by modeling clay and 0.08% MS-222 was delivered to the fish by a peristaltic pump at a flow rate of 2-3 ml per min. Multipoint time lapse imaging was achieved through Nikon elements software by manually setting large z-stacks for each field of view to account for sample drift during imaging. Depending on the experiment, time lapse images were acquired every 3-5 mins for up to 6 h at room temperature. To revive fish after multi-hour time lapse imaging, the peristaltic pump line was transferred to a bottle containing system water and fish were closely monitored for recovery. Data acquired from zebrafish that did not survive the intubation session were excluded from further analysis.

Staining

Alizarin Red S staining

Alizarin Red S stains calcium deposits allowing visualization of osteoblast-derived zebrafish scales. To visualize zebrafish scale development, live animals were stained for 20 min in a solution of 0.01% (wt/vol) Alizarin Red S (ACROS Organics, Cat #: 400480250) dissolved in system water and shielded from light, rinsed 3x, 5 mins in system water, then transferred back into fresh system water as described (Bensimon-Brito et al., 2016).

Immunofluorescence

520 Zebrafish were anesthetized in a solution of 0.012% MS-222 in system water for 2 min.
521 Approximately 30 scales were plucked and transferred to 1.5 mL tubes containing 375 µl
522 1xPBS. For fixation, 125 µl of 16% paraformaldehyde (PFA) was added to achieve a final 4%
523 PFA solution. Scales were incubated for 20 min at room temperature on a gently rotating
524 platform. PFA was washed out by carefully removing the fixation solution and replacing it with
525 400 µl of 0.2% PBST (1xPBS + 0.2% Triton X-100). Scales were washed 3x, 5 min with PBST
526 then blocked with blocking solution (10% normal goat serum in PBST) for 2-3 h at room
527 temperature. Blocking solution was removed, and 200 µl of primary antibody solution made up
528 in blocking solution was added. Primary antibodies used: Mouse monoclonal anti-SV2 (DSHB
529 Cat #: SV2, RRID:AB_2315387) at 1:50; or Rabbit polyclonal anti-GFP (Thermo Fisher
530 Scientific, Cat #: A11122, RRID:AB_221569) at 1:500. Scales were incubated in primary
531 antibody overnight at 4℃, protected from light. The next day, scales were washed 4x, 15 min
532 with PBST before adding secondary antibody made up in blocking solution. Secondary
533 antibodies used: Goat anti-Mouse Alexa Fluor 647 (Thermo Fisher Scientific, Cat #: A32728,
534 RRID:AB_2633277) at 1:500; or Goat anti-Rabbit Alexa Fluor 488 (Thermo Fisher Scientific, Cat
535 #: A32731, RRID:AB_2633280) at 1:1000. Scales were incubated for 2 h at room temperature,
536 protected from light. Secondary solution was washed out 4x, 15 min using PBST. To visualize
537 nuclei, 5 ng/µl DAPI (MilliporeSigma, Cat #: 508741) was added. DAPI was washed out 4x, 5
538 min using PBST. Scales were mounted epidermis-side up between a microscope slide and
539 coverslip in ProLong Gold (Thermo Fisher Scientific, Cat #: P36930). Imaging was performed
540 with a 40x (NA 1.3) oil immersion objective.
541
542 *Hybridization chain reaction*
543 HCR on adult zebrafish scales using a custom *piezo2* probe set (Molecular Instruments;
544 accession #: XM_021468270.1; set size: 20; amplifier: B3) was performed as described (Brown
545 et al., 2023). Scales were imaged with a 25x water immersion objective (N.A. 1.1)
546
547 *EdU labeling during scale regeneration*
548 Scales were plucked from adult *Tg(atoh1a:lifeact-egfp);Tg(sp7:mCherry)* zebrafish to induce
549 scale regeneration. Fish were returned to their tanks for recovery prior to EdU injection.
550 Regenerating fish were anesthetized in MS-222 and placed ventral side up on a sponge
551 situated under a dissecting microscope. 10 µl of 10 mM EdU (Thermo Fisher Scientific, Cat #:
552 C10640) was injected intraperitoneally in the region between the pelvic fins. Fish were
553 transferred back to system water for recovery. Approximately 20 h later, these fish had their
554 regenerating scales plucked and subjected to EdU staining following the manufacturer's
555 instructions. If downstream immunofluorescence was required, this was performed after EdU
556 detection. Stained scales were imaged with a 40x (NA 1.3) oil immersion objective.
557
558 **Image and statistical analysis**
559
560 *Image processing*
561 Image processing was performed using FIJI/ImageJ (Schindelin et al., 2012) or Imaris (Oxford
562 Instruments). Unless otherwise indicated, all images were gathered through z-stack acquisition
563 and displayed as maximum intensity projections. Throughout the figures, single channel images

of *Tg(atoh1a:lifeact-egfp)* are color-coded according to signal intensity using the "Green Fire Blue" lookup table in FIJI/ImageJ.

Cell counting & shape analysis

atoh1a+ cells were classified as dMCs or MCs as follows: Confocal z-stacks were max projected and the ImageJ "Cell Counter" function was used to manually classify *atoh1a+* cells as dMC or MC based on cell morphology. For shape analysis, max projected images were thresholded using Huang's algorithm. Using the "Analyze Particles…" function, circularity and roundness were calculated. In Figure 1N, "circular" cells were defined as those having circularity and roundness values >0.7.

Fluorescence intensity analysis

Fluorescence intensity of MCs and dMCs was calculated from confocal z-stacks acquired using identical settings by Corrected Total Cell Fluorescence (CTCF) in ImageJ. CTCF = Integrated Density – (Area of selected cell X Mean fluorescence of background readings).

z-depth analysis

For the z-depth analysis in Figure 5H, confocal z-stacks were acquired using a 25x water dipping objective (N.A. 1.1) and a z-step of 0.3 µm. The outer surface of the periderm was defined as a depth of 0. The distance from the center of the cell bodies of dMCs and MCs to the periderm surface was measured on reconstructed yz slices using the line tool in ImageJ.

Cell tracking

To quantify cell motility metrics, the trackmate plugin in ImageJ was used. z-stack acquired timelapse images were imported and made into max projections. To correct drift encountered during long term imaging acquisition, the Imagej plugin "correct 3D drift" was used to correct xy drift. Trackmate was opened and manual detection was performed by tracking individual cells of interest. The metrics calculated from trackmate (Total distance traveled, confinement ratio, etc) are explained https://imagej.net/plugins/trackmate/algorithms.

Statistical analysis

Statistical analysis and graphing were performed using R (R Core Team, 2023), MATLAB (MathWorks) or GraphPad (Prism). Statistical tests used and sample numbers are described in the corresponding figure legend.

ACKNOWLEDGEMENTS

We thank the LSB Aquatics staff for animal care and Dr. David Tobin for sharing zebrafish. The authors are grateful to all members of the Rasmussen lab for discussion, technical assistance, and support. The SV2 monoclonal antibody used in this study was obtained from the Developmental Studies Hybridoma Bank, created by the NICHD of the NIH and maintained at The University of Iowa, Department of Biology, Iowa City, IA 52242.

AUTHOR CONTRIBUTIONS

Evan W. Craig: Conceptualization, Investigation, Methodology, Visualization, Writing - Original Draft, Funding acquisition; **Erik C. Black**: Investigation, Methodology; **Camille E.A. Goo**:

Investigation, Methodology; **Avery Angell Swearer**: Investigation, Methodology; **Nathaniel G. Yee**: Investigation, Methodology; **Jeffrey P. Rasmussen**: Conceptualization, Investigation, Methodology, Validation, Supervision, Visualization, Writing - Original Draft, Funding acquisition.

COMPETING INTERESTS

No competing interests declared.

FUNDING

This work was funded in part by a Graduate Research Fellowship (DGE-2140004) from the National Science Foundation to EWC, an ISCRM Graduate Fellowship to ECB, R01-HD107108 from the Eunice Kennedy Shriver National Institute of Child Health and Human Development to JPR, and a New Investigator Award from the Fred Hutch/University of Washington/Seattle Children's Cancer Consortium, which is supported by the NIH/NCI Cancer Center Support Grant P30 CA015704, to JPR. JPR is a Washington Research Foundation Distinguished Investigator.

DATA AVAILABILITY

All data needed to evaluate the conclusions in the paper are present in the paper and/or the Supplementary Materials.

FIGURES AND FIGURE LEGENDS

Figure 1 - Craig et al.

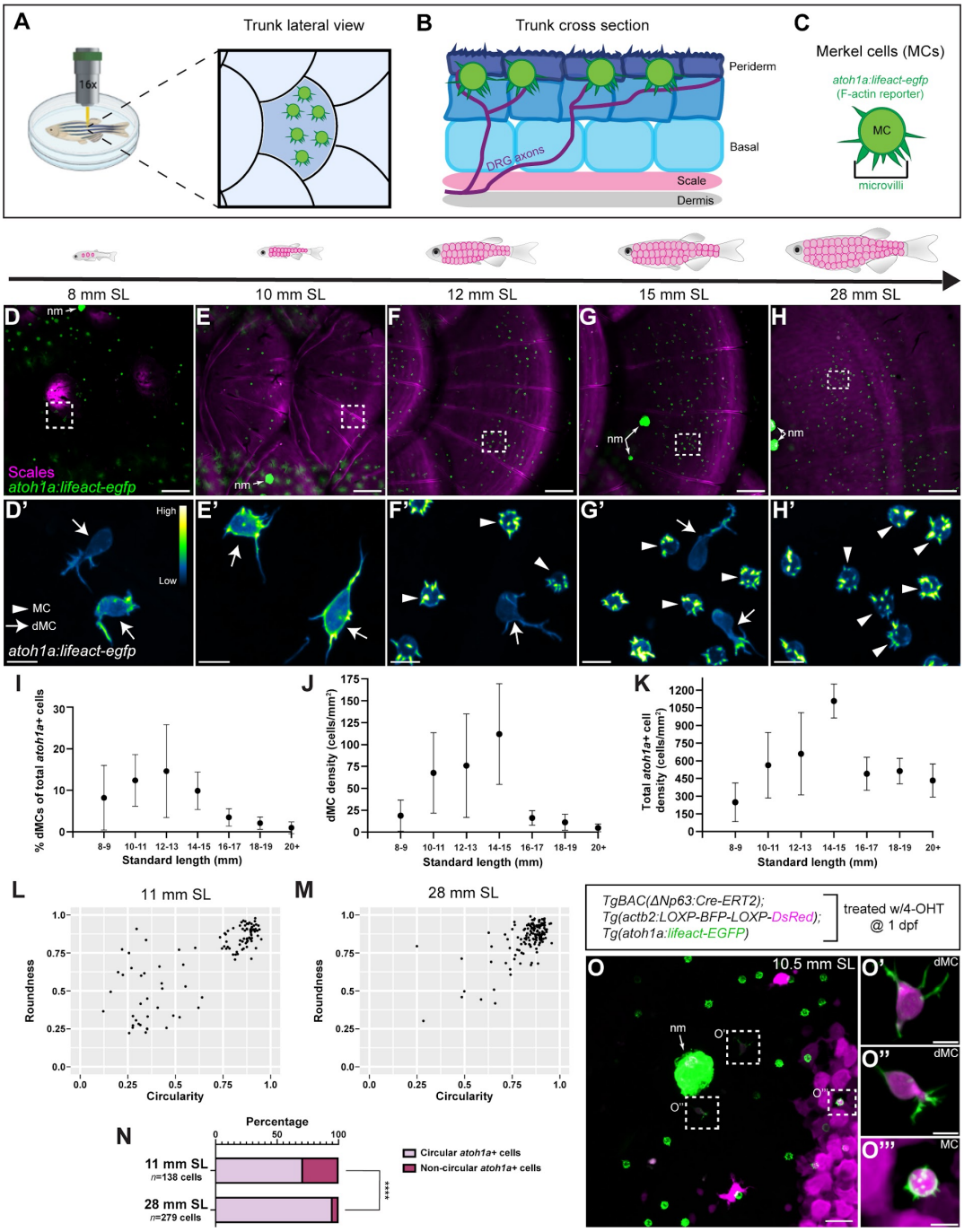

Figure 1. Identification of a transient, morphologically distinct population of keratinocyte-derived *atoh1a*+ cells during skin development

(A) Schematic depicting live-imaging methodology for visualizing MCs (green) within the epidermis atop scales along the lateral zebrafish trunk skin. **(B)** Illustration showing organization of adult zebrafish trunk skin in cross section. Note the stratified layers of keratinocytes above

634 the bony scale. Merkel cells are shown in green near the outermost epidermal layer. **(C)** The
635 *Tg(atoh1a:lifeact-egfp)* reporter allows visualization of the MC F-actin cytoskeleton, including
636 short and spiky microvilli structures. **(D-H)** Representative confocal micrographs of *atoh1a*+
637 MCs (green; *Tg(atoh1a:lifeact-egfp)*) and scales (magenta; Alizarin Red S staining) along the
638 lateral trunk in juvenile to adult zebrafish of the indicated stages. White dashed boxes indicate
639 regions magnified in (D'-H'). **(D'-H')** *Tg(atoh1a:lifeact-egfp)* signal intensity is color-coded using
640 the "Green Fire Blue" lookup table. MCs denoted by arrowheads, dMCs denoted by arrows. **(I)**
641 The percentage of *atoh1a*+ cells with dMC morphology out of total number of *atoh1a*+ cells
642 plotted against SL. Each dot represents the mean dMC percentage calculated from at least *n*=3
643 animals of that size range. For each individual zebrafish, multiple confocal micrographs were
644 acquired from the trunk region at 1.5x magnification and *atoh1a*+ cells were manually
645 categorized as "MC" or "dMC" based on morphology and grouped for input data to calculate the
646 dMC ratio shown. **(J)** Plot of dMC density relative to SL from the dataset analyzed in (I). **(K)** Plot
647 of total *atoh1a*+ cell density (dMCs and MCs) relative to SL from the dataset analyzed in (I).
648 **(L,M)** *atoh1a*+ cell shape analysis for animals of the indicated stages. Black dots represent
649 individual *atoh1a*+ cells that were assigned values for circularity and roundness after confocal
650 micrographs of *Tg(atoh1a:lifeact-egfp)* were thresholded to acquire *atoh1a*+ cell shape outlines.
651 Top right quadrant indicates cells with the most round and circular morphologies, indicative of
652 mature MCs. Cells falling outside of the top right quadrant possess less round and circular
653 morphologies, indicative of dMCs. *n*=100 randomly selected cells displayed for each stage. **(N)**
654 Stacked barcharts of *atoh1a*+ cell shape analysis performed in L-M. *atoh1a*+ cells in adult skin
655 have significantly more circular morphologies than *atoh1a*+ cells in juvenile skin (****, P<0.0001;
656 Fisher's Exact Test). **(O-O''')** Confocal micrographs of the trunk epidermis from a
657 *TgBAC(ΔNp63:Cre-ERT2); Tg(actb2:LOXP-BFP-LOXP-DsRed); Tg(atoh1a:lifeact-egfp)* juvenile
658 treated with 4-OHT at 1 dpf. Note the mosaic DsRed expression (magenta) in basal
659 keratinocytes and derivatives. DsRed+ dMCs shown in O'-O'', along with a DsRed+ MC in O'''
660 indicate both MC-types derive from a shared basal keratinocyte progenitor population. nm,
661 neuromasts containing clusters of *atoh1a*+ hair cells. Error bars in (I,J,K) display SD of mean.
662 Scale bars: 50 μm (D-H), 20 μm (O), and 5 μm (D'-H',O'-O''').

Figure 2 - Craig et al.

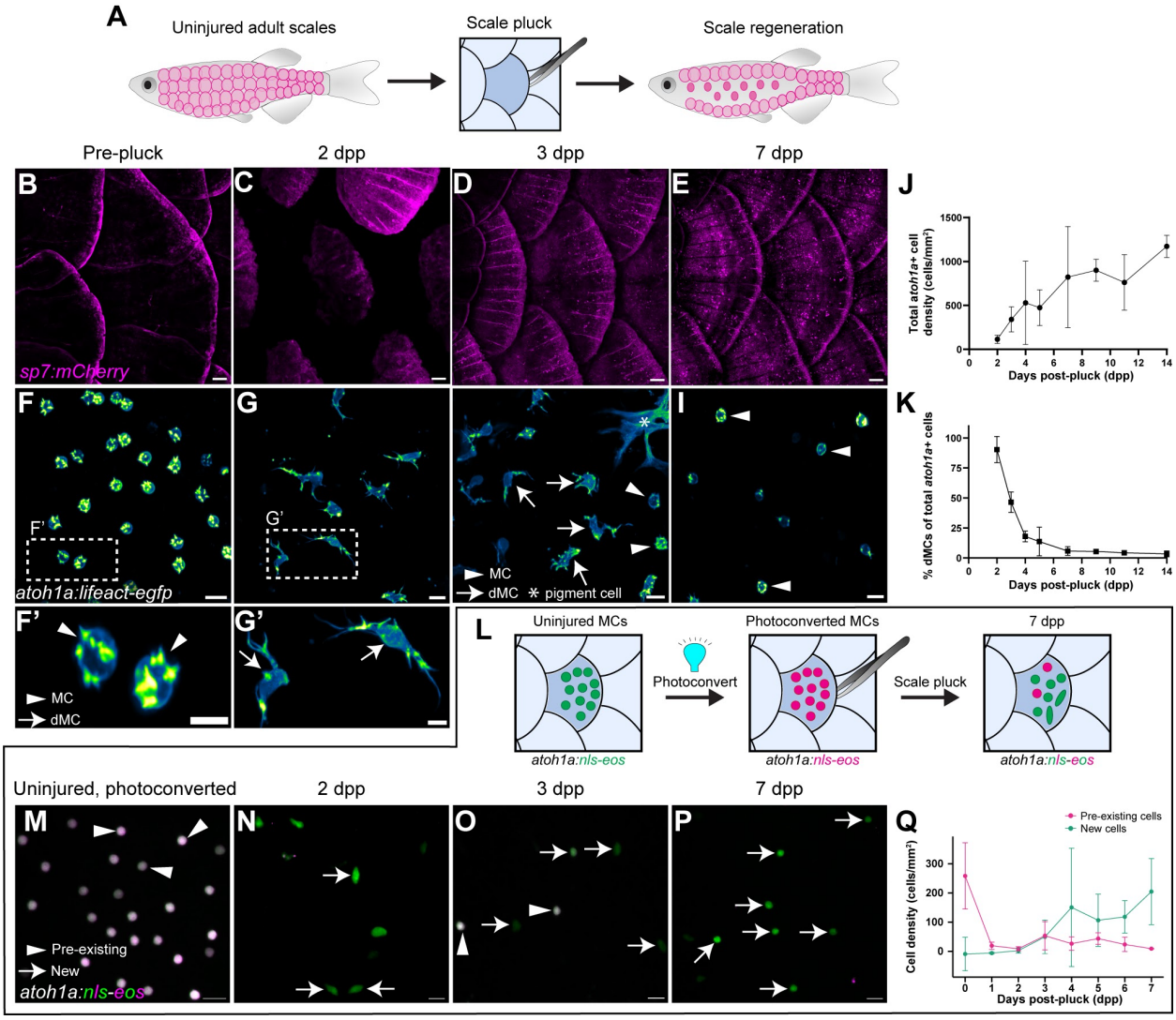

Figure 2. dMCs are the primary *atoh1a*+ cell type during the early stages of skin regeneration

(A) Illustration of the zebrafish scale pluck regeneration model. Forceps are used to physically "pluck" scales from the adult zebrafish trunk to induce injury and trigger regeneration of dermal scales and overlying epidermis. **(B-E)** Representative confocal micrographs of scale-forming osteoblasts (magenta; *Tg(sp7:mCherry)*) at the indicated stages of regeneration. **(F-I)** Representative confocal micrographs of *atoh1a*+ cell shapes within the scale epidermis at the indicated stages of scale regeneration. Yellow arrows denote MCs, green arrows denote dMCs, white arrow denotes an autofluorescent pigment cell. White dashed boxes indicate regions magnified in (F',G'). **(J)** Plot of total *atoh1a*+ cell density (dMCs and MCs) over the course of scale regeneration. Each dot represents confocal images collected and analyzed from multiple zebrafish of the corresponding timepoint (2-7 dpp, *n*=8-13; 9-14 dpp, *n*=2-4). **(K)** Quantification of dMC frequency during scale regeneration. Each dot represents the mean dMC frequency from the dataset analyzed in (J). **(L)** Illustration depicting the design of the *atoh1a*+ cell

678 photoconversion experiment. *Tg(atoh1a:nls-Eos)* expresses a nuclear-localized and
679 photoconvertible Eos protein in *atoh1a*+ cells (dMCs and MCs). *atoh1a*+ cells (green) in
680 uninjured scales are irreversibly photoconverted from green to magenta using UV light. Scales
681 containing photoconverted cells are then plucked to induce regeneration. Pre-existing *atoh1a*+
682 cells will contain photoconverted nls-Eos (magenta) in the new scale region whereas new
683 *atoh1a*+ cells will contain only non-photoconverted nls-Eos (green). **(M-P)** Representative
684 confocal micrographs of the photoconverted *Tg(atoh1a:nls-Eos)* scale epidermis pre-scale pluck
685 (M) and post-pluck (N-P). Arrowheads denote pre-existing cells (containing photoconverted nls-
686 Eos), arrows denote *de novo* generated cells (containing only non-photoconverted nls-Eos). **(Q)**
687 Quantification of pre-existing (magenta line) and new (green line) *atoh1a*+ cells from
688 photoconversion experiment at the indicated stages of regeneration. Each dot represents the
689 mean *atoh1a*+ cell density from *n*=3-4 fish. Scale bars, 100 µm (B-E), 10 µm (F-I), 5 µm (F', G'),
690 and 10 µm (M-P).

Figure 3 - Craig et al.

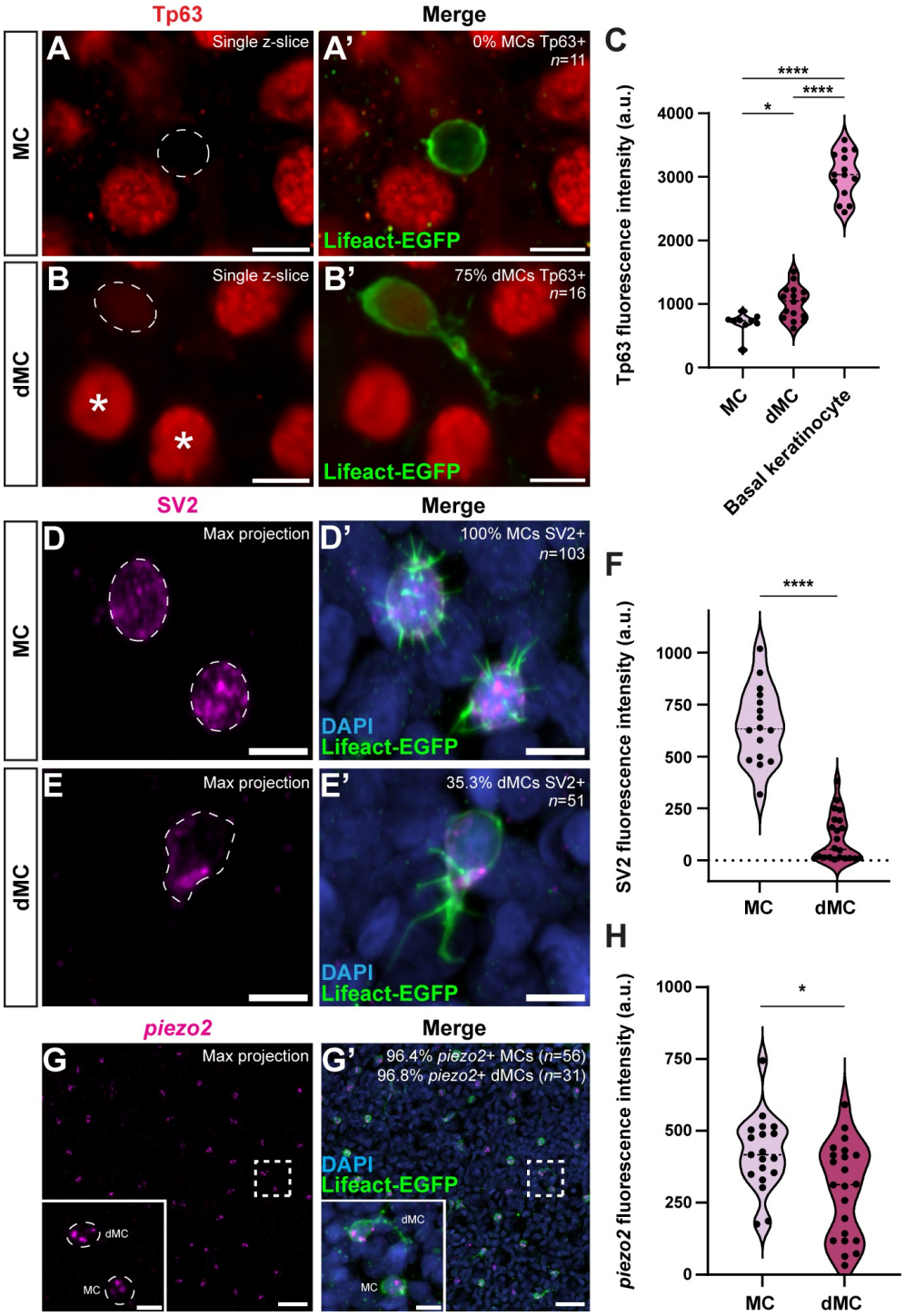

Figure 3. dMCs share molecular features with keratinocytes and MCs

(**A-B)** Representative micrographs of MCs and dMCs within the 5 dpp regenerating scale epidermis of a *Tg(atoh1a:lifeact-egfp)* adult visualized with anti-Tp63 (red) and anti-GFP (green) antibodies. Mature MCs are Tp63 negative (A) whereas dMCs are often weakly Tp63 positive

696 (B). Dashed lines outline the nuclei. Asterisks indicate basal keratinocyte nuclei. **(C)** Violin plots
697 of Tp63 staining intensity in MCs, dMCs, and basal keratinocytes. Confocal micrographs
698 acquired with identical imaging parameters were analyzed for Corrected Total Cell
699 Fluorescence (CTCF) measured in arbitrary units. Each dot represents an individual cell (*n*=9
700 MCs, *n*=16 dMCs, *n*=14 basal keratinocytes). A one-way ANOVA with post-hoc Tukey HSD test
701 was used to compare Tp63 staining levels between cell types. **(D-E)** Representative
702 micrographs showing MCs and dMCs within the 5 dpp regenerating scale epidermis of a
703 *Tg(atoh1a:lifeact-egfp)* adult stained with anti-SV2 (magenta) and anti-GFP (green) antibodies.
704 MCs are always SV2 positive (D), whereas some dMCs (E) are SV2 positive. Dashed lines
705 outline the cell bodies. **(F)** Violin plots of SV2 staining intensity quantified using CTCF in MCs
706 and dMCs. Each dot represents an individual cell (*n*=16 MCs, *n*=22 dMCs). A non-parametric
707 Mann-Whitney test was used to compare SV2 staining levels between cell types. **(G)**
708 Representative micrographs of MCs and dMCS within the 5 dpp regenerating scale epidermis of
709 a *Tg(atoh1a:lifeact-egfp)* adult stained with an anti-*piezo2* HCR probeset (magenta) and an anti-
710 GFP (green) antibody. Dashed box indicates region magnified in inset. Both MCs and dMCs are
711 *piezo2* positive. **(H)** Violin plots of *piezo2* HCR staining intensity in MCs and dMCs quantified
712 using CTCF. Each dot represents an individual cell (*n*=19 MCs, *n*=22 dMCs). A non-parametric
713 Mann-Whitney test was used to compare *piezo2* staining levels between cell types. *, P<0.05;
714 ****, P<0.0001. Scale bars, 5 µm (A-B,D-E,G inset) and 20 µm (G).

Figure 4 - Craig et al.

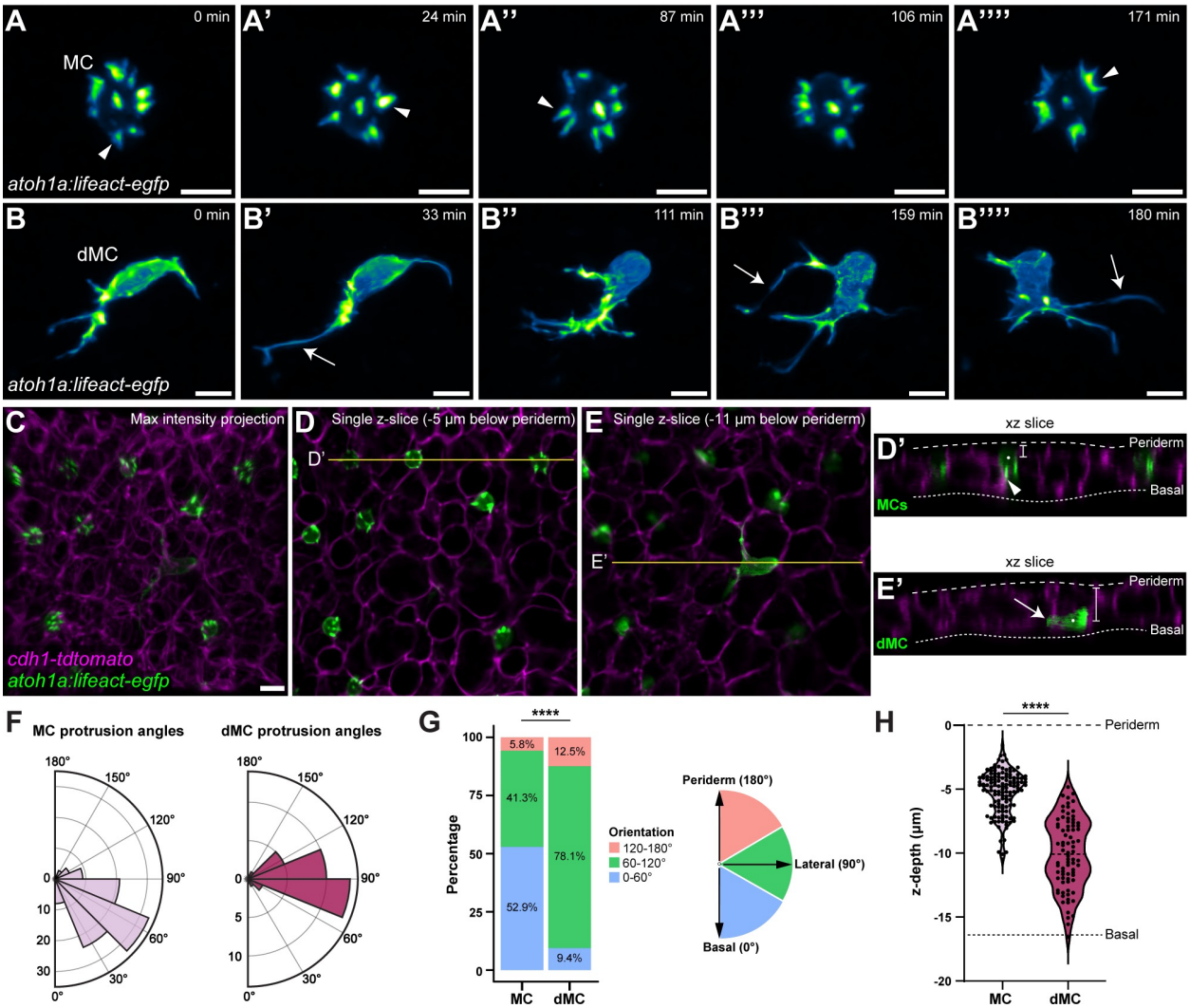

Figure 4. MC and dMC protrusions are dynamic and differentially polarized in the skin

(A-A'''') Still images of a timelapse of a single MC expressing *Tg(atoh1a:lifeact-egfp)*. White arrowheads point to microvilli extension, retraction, or merging events. **(B-B'''')** Still images of a timelapse of a single dMC visualized with *Tg(atoh1a:lifeact-egfp)*, image acquisition as described in (A). Note the longer, filopodial-like protrusions (white arrows) and highly amorphous cell body. **(C-E)** Representative maximum intensity projection (C) or individual z-slices (D,E) of the scale epidermis in an animal expressing *Tg(atoh1a:lifeact-egfp)* to label dMCs and MCs (green) and *(cdh1-tdTomato)* to label lateral cell membranes (magenta). **(D',E')** Reconstructed xz slices along the yellow lines in D and E. Dashed lines indicate the outer and inner epidermal margins. Note that the MCs in D' are located near the upper, periderm layer of the skin with basal facing protrusions (arrowhead), whereas the dMC in E' is located near the lower, basal layer of the skin with a lateral facing protrusion (arrow). Brightness and contrast were adjusted in (E,E') to better illustrate the dMC morphology. **(F)** Polar histograms of MC and dMC protrusion angles. Lifeact-EGFP+ protrusions that could be individually resolved in 3D were measured relative to the z-axis of the epidermis using the coordinate system diagrammed

731 in (G). Shaded regions indicate the number of protrusions falling in that angle range. Plots show
732 *n*=104 protrusions from 10 MCs and *n*=32 protrusions from 11 dMCs. **(G)** Stacked bar charts
733 depicting results in (F), with protrusions binned based on orientation. A χ^2 test was used to
734 compare between cell types (****, P<0.0001; χ^2 statistic, 18.9903). **(H)** Violin plots of z-depths of
735 MCs and dMCs measured relative to the periderm surface in the scale epidermis of *n*=130 MCs
736 and *n*=80 dMCs from 5 fish (11-12 mm SL). The average depth of the basal surface of basal
737 keratinocytes in the data set is indicated by a horizontal dashed line (-16.4 μm). A non-
738 parametric Mann-Whitney test was used to compare between cell types (****, P<0.0001). Scale
739 bars, 5 μm (A-C).

Figure 5 - Craig et al.

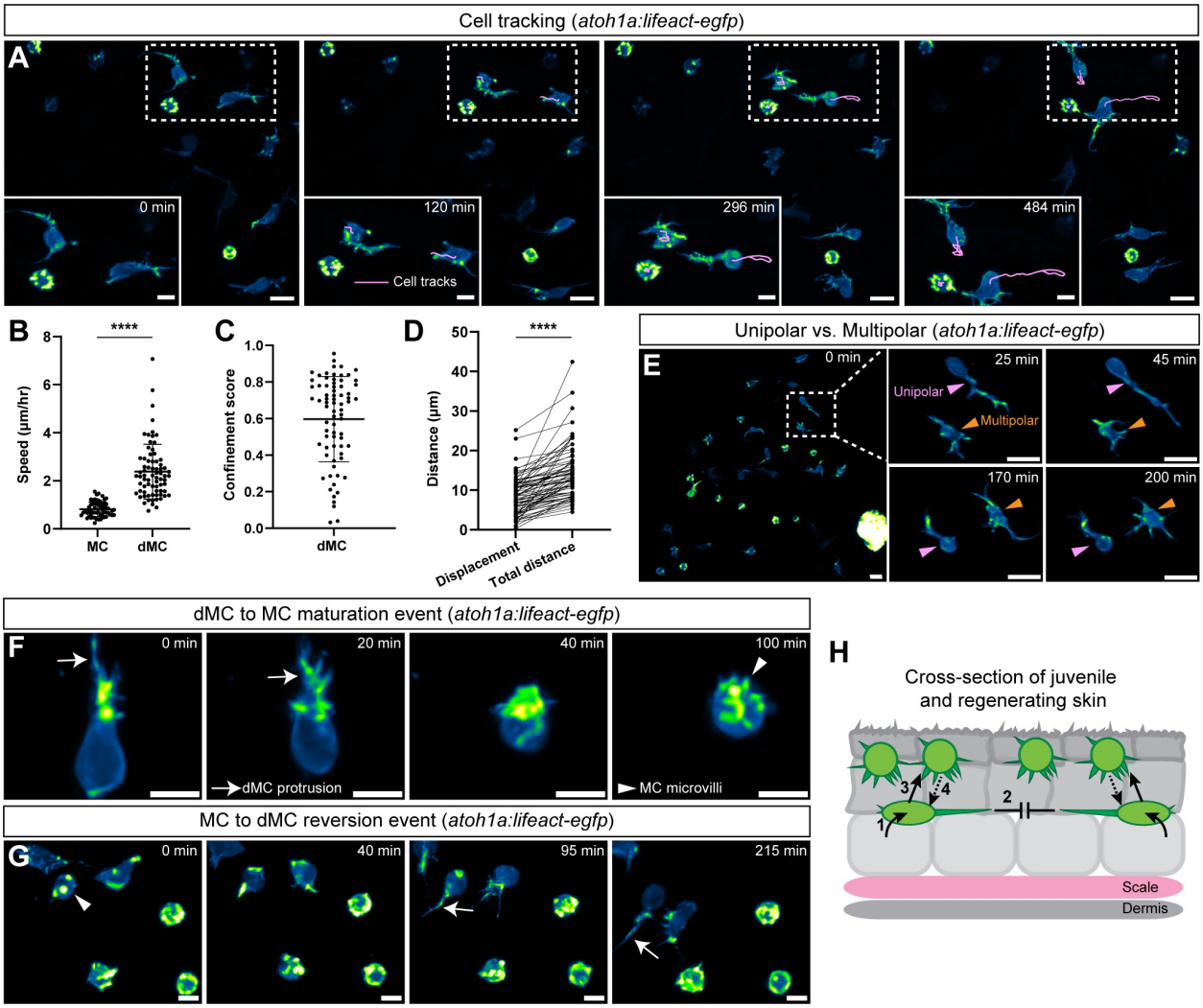

Figure 5. dMCs are motile cells that can directly mature into MCs in developing zebrafish skin

(A) Cell tracks (magenta) of individual MCs and dMCs traced over time. **(B)** Dot plot of cell speed (µm/hour) of individually tracked cells (*n*=60 MCs and *n*=74 dMCs). A non-parametric Mann-Whitney test was used to compare speed between cell types (****, P<0.0001). **(C)** Cell tracks scored for confinement ratio where values near 0 are indicative of confined movement and values near 1 are indicative of a linear trajectory (*n*=74 dMCs). **(D)** Dot plot of dMC track displacement, which measures the distance between the starting and ending point of each cell track, and total distance traveled (*n*=74 dMCs). A paired Mann-Whitney test was used to compare displacement and distance (****, P<0.0001). In (B-D), horizontal lines indicate the mean and error bars indicate the SD. **(E)** Representative timelapse stills from *Tg(atoh1a:lifeact-egfp)* expressing juvenile zebrafish skin. Magenta arrowheads highlight dMCs in their migratory configuration with unipolar protrusions. Orange arrowheads highlight dMCs in their exploratory or immotile configuration with multipolar protrusions. Note that individual cells can switch between the unipolar and multipolar configurations. **(F)** Representative timelapse stills of a dMC

to MC maturation event. Arrow indicates dMC protrusion retraction and arrowhead indicates formation of microvilli. Note the cell body switches from an ovoid to spherical shape during this transition. **(G)** Representative timelapse stills of a MC to dMC reversion event. Arrowhead indicates microvilli and arrow indicates filopodial-like protrusion extension. **(H)** Schematic depicting proposed model of dMC maturation events described in this study. (1) dMCs emerge in lower epidermal strata from *ΔNp63*+ basal keratinocyte progenitors; (2) dMCs are motile cells that migrate in the direction of their protrusions and can undergo contact inhibition upon encountering another dMC; (3) dMCs can directly adopt the mature MC morphology in upper epidermal strata; and (4) in rare instances, MCs can revert to a dMC morphology. Scale bars, 10 μm (A), 5 μm (A, insets), 10 μm (E, E, insets), and 5 μm (F,G).

Figure 6 - Craig et al.

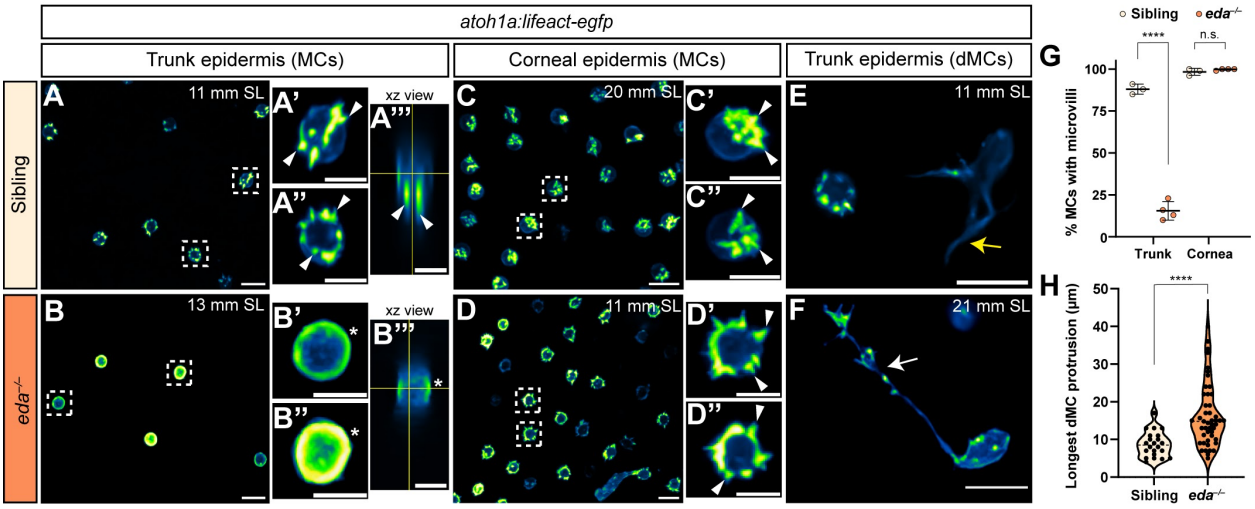

Figure 6. Genetic loss of Eda results in altered dMC and MC morphologies in trunk skin

(A,B) Representative confocal images of MCs within juvenile trunk epidermis of animals of the indicated genotypes and stages. Dashed boxes indicate cells magnified in (A',A'',B',B''). Arrowheads indicate microvilli and asterisks indicate intense Lifeact-EGFP signal forming a smooth, ring-like cortical structure evident in cross section in the *eda*$^{-/-}$ mutant epidermis. **(C,D)** Representative confocal images of MCs within corneal epidermis of animals of the indicated genotypes. Dashed boxes indicate cells magnified in (C',C'',D',D''). Arrowheads indicate microvilli. **(E,F)** Representative confocal images of dMCs within the trunk epidermis of animals of the indicated genotypes and stages. Yellow arrow in E indicates the longest protrusion on a dMC in *eda* sibling epidermis. White arrow in F indicates the longest protrusion on a dMC in *eda*$^{-/-}$ mutant epidermis. **(G)** Quantification of percentage of MCs with discernable microvilli in trunk or corneal epidermis of animals of the indicated genotypes. Each dot indicates a juvenile (9-20 mm SL) zebrafish of the respective genotype where a collection of images were analyzed (sibling trunk, *n*=386 cells from 3 fish; *eda*$^{-/-}$ trunk, *n*=235 cells from 4 fish; sibling cornea: *n*=169 cells from 4 fish; *eda*$^{-/-}$ cornea, *n*=332 cells from 4 fish). Fisher's exact test shows a significant difference between genotypes in the trunk but not cornea (****, P<0.0001; n.s., P=0.3413). **(H)** Violin plots of the longest dMC Lifeact-EGFP+ protrusion within the trunk epidermis of juveniles of the indicated genotypes. Each dot represents an individual cell (siblings, *n*=22 dMCs; *eda*$^{-/-}$, *n*=47 dMCs). A non-parametric Mann-Whitney test (****, P<0.0001) was used to compare between cell types. Scales bars, 10 µm (A-F), and 5 µm (A'-A''', B'-B''', C'-C'', D'-D'').

SUPPLEMENTAL FIGURE AND LEGEND

Figure S1 - Craig et al.

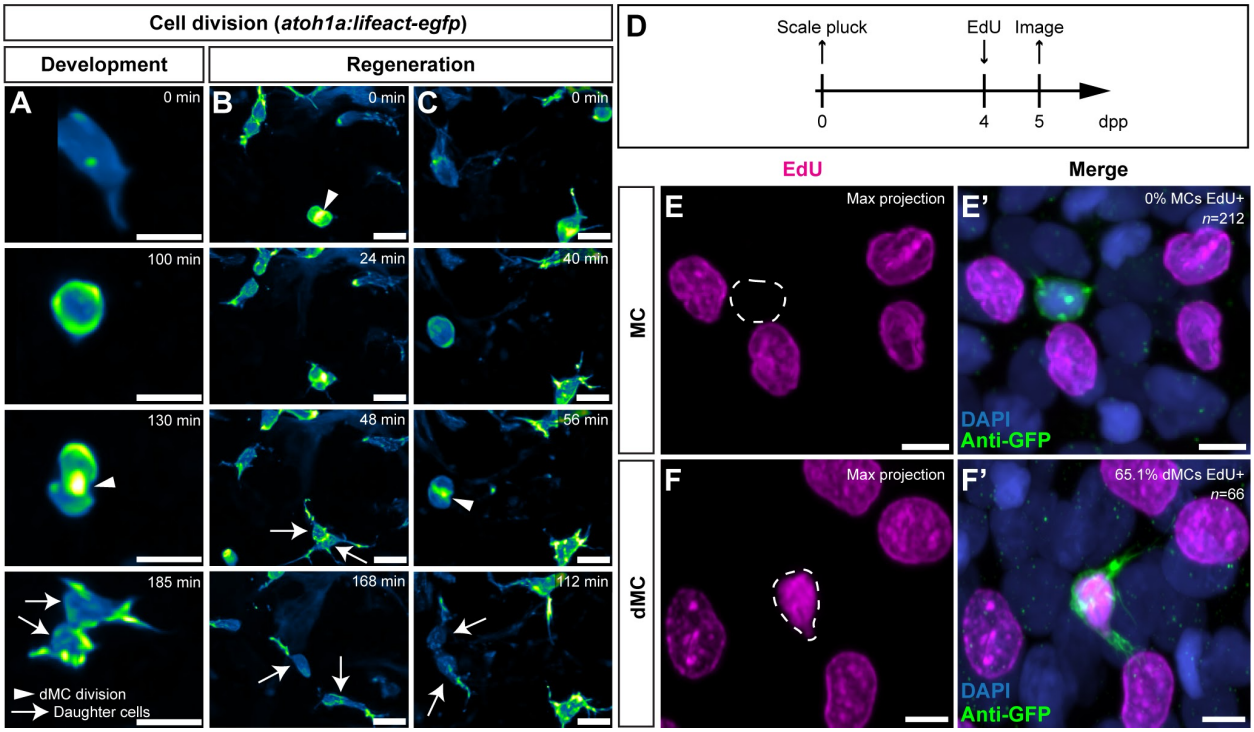

Figure S1: Differences in cell cycle state of dMCs and MCs

(A-C) Still images from timelapses showing cell divisions of dMCs expressing *Tg(atoh1a:lifeact-egfp)* in the juvenile (A) or regenerating scale epidermis (B,C). Arrowheads denote cytokinetic furrows and arrows denote daughter cells. **(D)** Experimental design of EdU administration and imaging during scale regeneration. **(E,F)** Representative confocal images of EdU and anti-GFP staining in regenerating *Tg(atoh1a:lifeact-egfp)* scales. White dashed lines indicate nuclear outlines. Scale bars, 10 µm (A-C) and 5 µm (E-F).

SUPPLEMENTAL MOVIE LEGENDS

Movie 1. Microvilli dynamics in zebrafish MCs. Timelapse movie of MCs expressing *Tg(atoh1a:lifeact-egfp)* in juvenile zebrafish skin. Note spike-like microvilli that extend, retract, and coalesce. Scale bar, 5 µm.

Movie 2. Actin dynamics in zebrafish dMCs. Timelapse movie of a dMC expressing *Tg(atoh1a:lifeact-egfp)* in juvenile zebrafish skin. Note thread-like filopodial protrusions that are highly dynamic. Scale bar, 10 µm.

Movie 3. Long-term imaging reveals dMC motile behaviors. 6 hour timelapse movie of MCs and dMCs expressing *Tg(atoh1a:lifeact-egfp)* in an intubated juvenile zebrafish. Manual cell tracks (white traces) show dMCs crawling in the direction of their protrusions while MCs remain largely stationary. Scale bar, 10 µm.

Movie 4. dMC-dMC contact inhibition. Timelapse of a dMC-dMC contact (indicated by arrow at time 0 min) that results in both cells migrating in opposing directions. Scale bars, 10 µm.

Movie 5. *In vivo* dMC cell division in juvenile zebrafish skin. Timelapse movie of a dMC expressing *Tg(atoh1a:lifeact-egfp)* undergoing cell division. In all dMC division events recorded, dividing dMCs retract a single unipolar protrusion, form a circular and actin-rich membrane, and undergo cytokinesis. Daughter cells then rapidly extend filopodial protrusions and migrate opposite from one another. Scale bar, 10 µm.

Movie 6. dMC to MC maturation event. Timelapse of single dMC expressing *Tg(atoh1a:lifeact-egfp)* that withdraws its filopodial protrusions, rounds its cell cortex, and extends small microvillar extensions as observed in mature MCs. Scale bar, 5 µm.

Movie 7. dMC behaviors during regeneration. Timelapse of the regenerating scale epidermis at 3 dpp in a *Tg(atoh1a:lifeact-egfp)* zebrafish. Labels indicate different dMC behaviors including maturation, motility, and cell death. Scale bar, 10 µm.

Movie 8. MC to dMC reversion event. Timelapse of developing *Tg(atoh1a:lifeact-egfp)* expressing zebrafish skin with a mix of MCs and dMCs in the field of view. Note a cell with a MC morphology begins to transition into a dMC-like cell with a long unipolar protrusion. Scale bar, 10 µm.

833 **REFERENCES**

834

835 **Aman, A. J., Fulbright, A. N. and Parichy, D. M.** (2018). Wnt/β-catenin regulates an ancient
836 signaling network during zebrafish scale development. *Elife* **7**,.
837 **Bakkers, J., Hild, M., Kramer, C., Furutani-Seiki, M. and Hammerschmidt, M.** (2002).
838 Zebrafish DeltaNp63 is a direct target of Bmp signaling and encodes a transcriptional
839 repressor blocking neural specification in the ventral ectoderm. *Dev Cell* **2**, 617–627.
840 **Barr-Gillespie, P.-G.** (2015). Assembly of hair bundles, an amazing problem for cell biology.
841 *Mol Biol Cell* **26**, 2727–2732.
842 **Becker, J. C., Stang, A., DeCaprio, J. A., Cerroni, L., Lebbé, C., Veness, M. and Nghiem, P.**
843 (2017). Merkel cell carcinoma. *Nat Rev Dis Primers* **3**, 17077.
844 **Bensimon-Brito, A., Cardeira, J., Dionísio, G., Huysseune, A., Cancela, M. L. and Witten,**
845 **P. E.** (2016). Revisiting in vivo staining with alizarin red S--a valuable approach to
846 analyse zebrafish skeletal mineralization during development and regeneration. *BMC*
847 *Dev Biol* **16**, 2.
848 **Boot, P. M., Rowden, G. and Walsh, N.** (1992). The distribution of Merkel cells in human fetal
849 and adult skin. *Am J Dermatopathol* **14**, 391–396.
850 **Brown, T. L., Horton, E. C., Craig, E. W., Goo, C. E. A., Black, E. C., Hewitt, M. N., Yee, N.**
851 **G., Fan, E. T., Raible, D. W. and Rasmussen, J. P.** (2023). Dermal appendage-
852 dependent patterning of zebrafish atoh1a+ Merkel cells. *Elife* **12**, e85800.
853 **Burgess, P. R., English, K. B., Horch, K. W. and Stensaas, L. J.** (1974). Patterning in the
854 regeneration of type I cutaneous receptors. *J Physiol* **236**, 57–82.
855 **Cai, E., Marchuk, K., Beemiller, P., Beppler, C., Rubashkin, M. G., Weaver, V. M., Gérard,**
856 **A., Liu, T.-L., Chen, B.-C., Betzig, E., et al.** (2017). Visualizing dynamic microvillar
857 search and stabilization during ligand detection by T cells. *Science* **356**, eaal3118.
858 **Cox, B. D., De Simone, A., Tornini, V. A., Singh, S. P., Di Talia, S. and Poss, K. D.** (2018). In
859 Toto Imaging of Dynamic Osteoblast Behaviors in Regenerating Skeletal Bone. *Curr Biol*
860 **28**, 3937-3947.e4.
861 **Cronan, M. R., Matty, M. A., Rosenberg, A. F., Blanc, L., Pyle, C. J., Espenschied, S. T.,**
862 **Rawls, J. F., Dartois, V. and Tobin, D. M.** (2018). An explant technique for high-
863 resolution imaging and manipulation of mycobacterial granulomas. *Nat Methods* **15**,
864 1098–1107.
865 **Daghfous, G., Auclair, F., Blumenthal, F., Suntres, T., Lamarre-Bourret, J., Mansouri, M.,**
866 **Zielinski, B. and Dubuc, R.** (2020). Sensory cutaneous papillae in the sea lamprey
867 (Petromyzon marinus L.): I. Neuroanatomy and physiology. *J Comp Neurol* **528**, 664–
868 686.
869 **De Simone, A., Evanitsky, M. N., Hayden, L., Cox, B. D., Wang, J., Tornini, V. A., Ou, J.,**
870 **Chao, A., Poss, K. D. and Di Talia, S.** (2021). Control of osteoblast regeneration by a
871 train of Erk activity waves. *Nature* **590**, 129–133.
872 **Düring, M. V. and Andres, K. H.** (1976). The ultrastructure of taste and touch receptors of the
873 frog's taste organ. *Cell Tissue Res* **165**, 185–198.
874 **English, K. B.** (1974). Cell types in cutaneous type I mechanoreceptors (Haarscheiben) and
875 their alterations with injury. *Am J Anat* **141**, 105–126.
876 **English, K. B.** (1977). Morphogenesis of Haarscheiben in rats. *J Invest Dermatol* **69**, 58–67.
877 **Felker, A., Nieuwenhuize, S., Dolbois, A., Blazkova, K., Hess, C., Low, L. W. L., Burger, S.,**
878 **Samson, N., Carney, T. J., Bartunek, P., et al.** (2016). In vivo performance and
879 properties of tamoxifen metabolites for CreERT2 control. *PLoS One* **11**, e0152989.
880 **Garant, P. R., Feldman, J., Cho, M. I. and Cullen, M. R.** (1980). Ultrastructure of Merkel cells
881 in the hard palate of the squirrel monkey (Saimiri sciureus). *Am J Anat* **157**, 155–167.
882 **Girard, D., Laverdet, B., Buhé, V., Trouillas, M., Ghazi, K., Alexaline, M. M., Egles, C.,**

883 **Misery, L., Coulomb, B., Lataillade, J.-J., et al.** (2017). Biotechnological Management
884 of Skin Burn Injuries: Challenges and Perspectives in Wound Healing and Sensory
885 Recovery. *Tissue Eng Part B Rev* **23**, 59–82.
886 **Guzman, A., Ramos-Balderas, J. L., Carrillo-Rosas, S. and Maldonado, E.** (2013). A stem
887 cell proliferation burst forms new layers of P63 expressing suprabasal cells during
888 zebrafish postembryonic epidermal development. *Biol. Open* **2**, 1179–1186.
889 **Hahn, J. M., Combs, K. A., Lloyd, C. M., McFarland, K. L., Boyce, S. T. and Supp, D. M.**
890 (2019). Identification of Merkel cells associated with neurons in engineered skin
891 substitutes after grafting to full thickness wounds. *PLoS One* **14**, e0213325.
892 **Halata, Z.** (1975). The mechanoreceptors of the mammalian skin ultrastructure and
893 morphological classification. *Advances In Anatomy, Embryology and Cell Biology* **50**, 3–
894 77.
895 **Harms, P. W., Harms, K. L., Moore, P. S., DeCaprio, J. A., Nghiem, P., Wong, M. K. K.,**
896 **Brownell, I., and International Workshop on Merkel Cell Carcinoma Research**
897 **(IWMCC) Working Group** (2018). The biology and treatment of Merkel cell carcinoma:
898 current understanding and research priorities. *Nat Rev Clin Oncol* **15**, 763–776.
899 **Harris, M. P., Rohner, N., Schwarz, H., Perathoner, S., Konstantinidis, P. and Nüsslein-**
900 **Volhard, C.** (2008). Zebrafish eda and edar mutants reveal conserved and ancestral
901 roles of ectodysplasin signaling in vertebrates. *PLoS Genet* **4**, e1000206.
902 **Hartschuh, W., Weihe, E. and Reinecke, M.** (1986). The Merkel Cell. In *Biology of the*
903 *Integument: 2 Vertebrates* (ed. Bereiter-Hahn, J.), Matoltsy, A. G.), and Richards, K. S.),
904 pp. 605–620. Berlin, Heidelberg: Springer Berlin Heidelberg.
905 **Hashimoto, K.** (1972). Fine structure of Merkel cell in human oral mucosa. *J Invest Dermatol*
906 **58**, 381–387.
907 **Horch, K.** (1982). The influence of mechanoreceptor structures on regenerating sensory axons
908 after cutaneous nerve transection in the cat. *Neurosci Lett* **32**, 281–284.
909 **Iggo, A. and Muir, A. R.** (1969). The structure and function of a slowly adapting touch
910 corpuscle in hairy skin. *J Physiol* **200**, 763–796.
911 **Iwasaki, M., Kuroda, J., Kawakami, K. and Wada, H.** (2018). Epidermal regulation of bone
912 morphogenesis through the development and regeneration of osteoblasts in the
913 zebrafish scale. *Dev Biol* **437**, 105–119.
914 **Kim, D. K. and Holbrook, K. A.** (1995). The appearance, density, and distribution of Merkel
915 cells in human embryonic and fetal skin: their relation to sweat gland and hair follicle
916 development. *J Invest Dermatol* **104**, 411–416.
917 **Kobayashi, I., Kobayashi-Sun, J., Kim, A. D., Pouget, C., Fujita, N., Suda, T. and Traver, D.**
918 (2014). Jam1a-Jam2a interactions regulate haematopoietic stem cell fate through Notch
919 signalling. *Nature* **512**, 319–23.
920 **Landmann, L. and Halata, Z.** (1980). Merkel cells and nerve endings in the labial epidermis of
921 a lizard. *Cell Tissue Res* **210**, 353–357.
922 **Lane, E. B. and Whitear, M.** (1977). On the occurrence of Merkel cells in the epidermis of
923 teleost fishes. *Cell and Tissue Research* **182**, 235–46.
924 **Lee, H. and Kimelman, D.** (2002). A dominant-negative form of p63 is required for epidermal
925 proliferation in zebrafish. *Dev Cell* **2**, 607–616.
926 **Meenderink, L. M., Gaeta, I. M., Postema, M. M., Cencer, C. S., Chinowsky, C. R.,**
927 **Krystofiak, E. S., Millis, B. A. and Tyska, M. J.** (2019). Actin Dynamics Drive
928 Microvillar Motility and Clustering during Brush Border Assembly. *Dev Cell* **50**, 545-
929 556.e4.
930 **Merot, Y. and Saurat, J. H.** (1988). Proliferation of Merkel cells in the skin. *Acta Derm Venereol*
931 **68**, 366–367.
932 **Moll, R., Moll, I. and Franke, W. W.** (1984). Identification of Merkel cells in human skin by
933 specific cytokeratin antibodies: changes of cell density and distribution in fetal and adult

934 plantar epidermis. *Differentiation* **28**, 136–154.
935 **Moll, I., Zieger, W. and Schmelz, M.** (1996). Proliferative merkel cells were not detected in
936 human skin. *Arch Dermatol Res* **288**, 184–187.
937 **Morrison, K. M., Miesegaes, G. R., Lumpkin, E. A. and Maricich, S. M.** (2009). Mammalian
938 Merkel cells are descended from the epidermal lineage. *Developmental Biology* **336**, 76–
939 83.
940 **Nakafusa, J., Narisawa, Y., Shinogi, T., Taira, K., Tanaka, T., Inoue, T. and Misago, N.**
941 (2006). Changes in the number of Merkel cells with the hair cycle in hair discs on rat
942 back skin. *Br J Dermatol* **155**, 883–889.
943 **Nurse, C. A., Macintyre, L. and Diamond, J.** (1984). Reinnervation of the rat touch dome
944 restores the Merkel cell population reduced after denervation. *Neuroscience* **13**, 563–
945 571.
946 **Ostrowski, S. M., Wright, M. C., Bolock, A. M., Geng, X. and Maricich, S. M.** (2015). Ectopic
947 Atoh1 expression drives Merkel cell production in embryonic, postnatal and adult mouse
948 epidermis. *Development* **142**, 2533–2544.
949 **Parichy, D. M., Elizondo, M. R., Mills, M. G., Gordon, T. N. and Engeszer, R. E.** (2009).
950 Normal table of postembryonic zebrafish development: staging by externally visible
951 anatomy of the living fish. *Developmental Dynamics* **238**, 2975–3015.
952 **Pickett, S. B., Thomas, E. D., Sebe, J. Y., Linbo, T., Esterberg, R., Hailey, D. W. and Raible,**
953 **D. W.** (2018). Cumulative mitochondrial activity correlates with ototoxin susceptibility in
954 zebrafish mechanosensory hair cells. *Elife* **7**,.
955 **R Core Team** (2023). *R: A Language and Environment for Statistical Computing*. Vienna,
956 Austria: R Foundation for Statistical Computing.
957 **Rangel-Huerta, E., Guzman, A. and Maldonado, E.** (2021). The dynamics of epidermal
958 stratification during post-larval development in zebrafish. *Dev Dyn* **250**, 175–190.
959 **Richardson, R., Metzger, M., Knyphausen, P., Ramezani, T., Slanchev, K., Kraus, C.,**
960 **Schmelzer, E. and Hammerschmidt, M.** (2016). Re-epithelialization of cutaneous
961 wounds in adult zebrafish combines mechanisms of wound closure in embryonic and
962 adult mammals. *Development* **143**, 2077–88.
963 **Sadier, A., Viriot, L., Pantalacci, S. and Laudet, V.** (2014). The ectodysplasin pathway: from
964 diseases to adaptations. *Trends Genet* **30**, 24–31.
965 **Schindelin, J., Arganda-Carreras, I., Frise, E., Kaynig, V., Longair, M., Pietzsch, T.,**
966 **Preibisch, S., Rueden, C., Saalfeld, S., Schmid, B., et al.** (2012). Fiji: an open-source
967 platform for biological-image analysis. *Nature Methods* **9**, 676–82.
968 **Sekerková, G., Zheng, L., Loomis, P. A., Changyaleket, B., Whitlon, D. S., Mugnaini, E.**
969 **and Bartles, J. R.** (2004). Espins are multifunctional actin cytoskeletal regulatory
970 proteins in the microvilli of chemosensory and mechanosensory cells. *J Neurosci* **24**,
971 5445–5456.
972 **Sekerková, G., Zheng, L., Loomis, P. A., Mugnaini, E. and Bartles, J. R.** (2006). Espins and
973 the actin cytoskeleton of hair cell stereocilia and sensory cell microvilli. *Cell Mol Life Sci*
974 **63**, 2329–2341.
975 **Sharkova, M., Chow, E., Erickson, T. and Hocking, J. C.** (2023). The morphological and
976 functional diversity of apical microvilli. *J Anat* **242**, 327–353.
977 **Singh, S. P., Holdway, J. E. and Poss, K. D.** (2012). Regeneration of amputated zebrafish fin
978 rays from de novo osteoblasts. *Developmental Cell* **22**, 879–86.
979 **Sire, J.-Y., Quilhac, A., Bourguignon, J. and Allizard, F.** (1997). Evidence for participation of
980 the epidermis in the deposition of superficial layer of scales in zebrafish (Danio rerio): A
981 SEM and TEM study. *J Morphol* **231**, 161–174.
982 **Stella, M., Calcagni, M., Teich-Alasia, S., Ramieri, G., Cellino, G. and Panzica, G.** (1994).
983 Sensory endings in skin grafts and scars after extensive burns. *Burns* **20**, 491–495.
984 **Tachibana, T. and Ishizeki, K.** (1981). Merkel cell development in the wound healing in the

985 labial mucosa of adult rabbits. *Arch Histol Jpn* **44**, 151–165.
986 **Tachibana, T. and Nawa, T.** (1980). Merkel cell differentiation in the labial mucous epithelium
987 of the rabbit. *J Anat* **131**, 145–155.
988 **Tachibana, T., Yamamoto, H., Takahashi, N., Kamegai, T., Shibanai, S., Iseki, H. and**
989 **Nawa, T.** (1997). Polymorphism of Merkel cells in the rodent palatine mucosa:
990 immunohistochemical and ultrastructural studies. *Arch Histol Cytol* **60**, 379–389.
991 **Tachibana, T., Kamegai, T., Takahashi, N. and Nawa, T.** (1998). Evidence for polymorphism
992 of Merkel cells in the adult human oral mucosa. *Arch Histol Cytol* **61**, 115–124.
993 **Takahashi-Iwanaga, H.** (2003). The Three-Dimensional Microanatomy of Merkel Cells. In *The*
994 *Merkel Cell* (ed. Baumann, K. I.), Halata, Z.), and Moll, I.), pp. 7–12. Berlin, Heidelberg:
995 Springer Berlin Heidelberg.
996 **Takahashi-Iwanaga, H. and Abe, K.** (2001). Scanning electron microscopic observation of
997 Merkel cells in the lamprey epidermis. *Kaibogaku Zasshi* **76**, 375–380.
998 **Toyoshima, K., Seta, Y., Takeda, S. and Harada, H.** (1998). Identification of Merkel cells by an
999 antibody to villin. *Journal of Histochemistry & Cytochemistry* **46**, 1329–34.
1000 **Vaigot, P., Pisani, A., Darmon, Y. M. and Ortonne, J. P.** (1987). The majority of epidermal
1001 Merkel cells are non-proliferative: a quantitative immunofluorescence analysis. *Acta*
1002 *Derm Venereol* **67**, 517–520.
1003 **Van Keymeulen, A., Mascre, G., Youseff, K. K., Harel, I., Michaux, C., De Geest, N.,**
1004 **Szpalski, C., Achouri, Y., Bloch, W., Hassan, B. A., et al.** (2009). Epidermal
1005 progenitors give rise to Merkel cells during embryonic development and adult
1006 homeostasis. *Journal of Cell Biology* **187**, 91–100.
1007 **Weber, M., Nguyen, M. B., Li, M. Y., Flora, P., Shuda, M. and Ezhkova, E.** (2023). Merkel
1008 Cell Polyomavirus T Antigen-Mediated Reprogramming in Adult Merkel Cell Progenitors.
1009 *J Invest Dermatol* S0022-202X(23)02120–6.
1010 **Whitear, M.** (1989). Merkel cells in lower vertebrates. *Archivum Histologicum Japonicum* **52**
1011 **Suppl**, 415–22.
1012 **Whitear, M. and Lane, E. B.** (1981). Fine structure of Merkel cells in lampreys. *Cell and Tissue*
1013 *Research* **220**, 139–51.
1014 **Woo, S.-H., Lumpkin, E. A. and Patapoutian, A.** (2015). Merkel cells and neurons keep in
1015 touch. *Trends Cell Biol* **25**, 74–81.
1016 **Wright, M. C., Logan, G. J., Bolock, A. M., Kubicki, A. C., Hemphill, J. A., Sanders, T. A.**
1017 **and Maricich, S. M.** (2017). Merkel cells are long-lived cells whose production is
1018 stimulated by skin injury. *Dev Biol* **422**, 4–13.
1019 **Xiao, Y., Williams, J. S. and Brownell, I.** (2014). Merkel cells and touch domes: more than
1020 mechanosensory functions? *Exp Dermatol* **23**, 692–695.
1021 **Xu, C., Volkery, S. and Siekmann, A. F.** (2015). Intubation-based anesthesia for long-term
1022 time-lapse imaging of adult zebrafish. *Nature Protocols* **10**, 2064–73.
1023 **Yamashita, Y., Toida, K. and Ogawa, H.** (1993). Observation of Merkel cells with scanning
1024 electron microscopy. *Neurosci Lett* **159**, 155–158.